

UCLA

UCLA Previously Published Works

Title

Multimomics reveals glutathione metabolism as a driver of bimodality during stem cell aging.

Permalink

<https://escholarship.org/uc/item/00g0453f>

Journal

Cell Metabolism, 35(3)

Authors

Benjamin, Daniel

Brett, Jamie

Both, Pieter

et al.

Publication Date

2023-03-07

DOI

10.1016/j.cmet.2023.02.001

Peer reviewed



Published in final edited form as:

Cell Metab. 2023 March 07; 35(3): 472–486.e6. doi:10.1016/j.cmet.2023.02.001.

Multiomics reveals glutathione metabolism as a driver of bimodality during stem cell aging

Daniel I. Benjamin^{1,2,#}, Jamie O. Brett^{1,2,3,4,#}, Pieter Both^{1,2,3}, Joel S. Benjamin^{1,2}, Heather L. Ishak², Jengmin Kang^{1,2}, Soochi Kim^{1,2}, Mingyu Chung^{1,2}, Marina Arjona^{1,2}, Christopher W. Nutter², Jenna H. Tan², Ananya K. Krishnan², Hunter Dulay², Sharon M. Louie⁵, Antoine de Morree^{1,2,6}, Daniel K. Nomura⁵, Thomas A. Rando^{*,1,2,7,8,9}

¹Department of Neurology and Neurological Sciences, Stanford University School of Medicine, Stanford, CA, USA

²Paul F. Glenn Laboratories for the Biology of Aging, Stanford University School of Medicine, Stanford, CA, SA

³Stem Cell Biology and Regenerative Medicine Graduate Program, Stanford University School of Medicine, Stanford, CA, USA

⁴Medical Scientist Training Program, Stanford University School of Medicine, Stanford, CA, USA

⁵Department of Nutritional Sciences and Toxicology, University of California, Berkeley, Berkeley, CA 94720, USA.

⁶Current Address: Department of Biomedicine, Aarhus University

⁷Neurology Service, Veterans Affairs Palo Alto Healthcare System, Palo Alto, CA, USA

⁸Current address: Broad Stem Cell Research Center, University of California Los Angeles, Los Angeles, CA USA

⁹Lead Contact

Summary

With age, skeletal muscle stem cells (MuSCs) activate out of quiescence more slowly and with increased death, leading to defective muscle repair. To explore the molecular underpinnings of these defects, we combined multiomics, single-cell measurements, and functional testing of MuSCs from young and old mice. The multiomics approach allowed us to assess which changes are causal, which are compensatory, and which are simply correlative. We identified glutathione (GSH) metabolism as perturbed in old MuSCs, with both causal and compensatory components. Contrary to young MuSCs, old MuSCs exhibit a population dichotomy composed of GSH^{high} cells

*Correspondence to trando@mednet.ucla.edu.

#These authors contributed equally

Author contributions

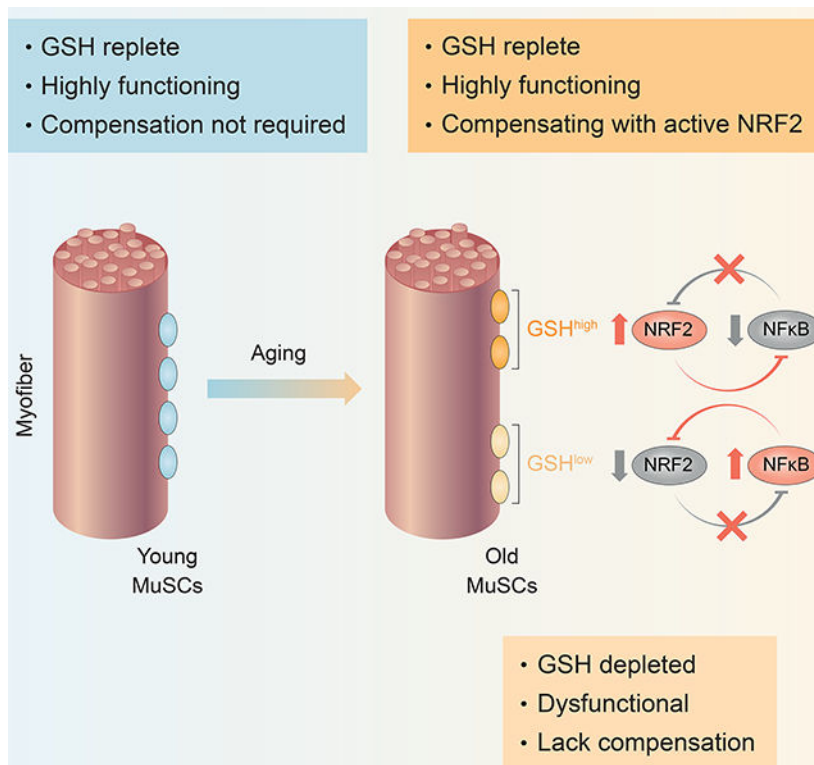
D.I.B. and J.O.B. designed the studies and carried out experiments with assistance from P.B., J.S.B., M.A., C.W.N., H.D., S.M.L., and D.K.N. and with guidance from T.A.R. throughout. D.I.B. and J.O.B. interpreted the results with guidance and input from T.A.R. D.I.B., J.O.B., and T.A.R. wrote the manuscript and assembled the data with assistance from P.B.

Declaration of Interests

The authors declare no competing interests

(comparable to young MuSCs) and GSH^{low} cells with impaired functionality. Mechanistically, we show that antagonism between NRF2 and NF- κ B maintains this bimodality. Experimental manipulation of GSH levels altered the functional dichotomy of aged MuSCs. These findings identify a novel mechanism of stem cell aging and highlight glutathione metabolism as an accessible target for reversing MuSC aging.

Graphical Abstract



eTOC Blurp

The present study uses a multiomic analysis to uncover a novel mechanism that underlies stem cell aging. Benjamin et al report how GSH metabolism is altered with age in a bimodal manner creating two functionally distinct metabolic subpopulations of aged cells.

Introduction

Aging is due to the combination of accumulating stressors and declining homeostatic reserves^{1,2}. Aging is thus a disorderly process, a failure of healthy systems signaling and coordination³⁻⁵. Furthermore, aging is complex, multifactorial, and arguably impossible to completely elucidate (not all the unknowns are known); this is considered a major barrier to the development of interventions to improve lifespan and healthspan⁶⁻¹⁰.

This situation is exemplified in the aging of skeletal muscle stem cells (MuSCs), a regenerative adult stem cell population that declines significantly in muscle repair ability during aging¹¹. Numerous intrinsic and extrinsic pathways that contribute to old MuSC

impairment have been identified, and ever more are being discovered; strategies for this discovery have ranged from specific hypothesis testing to unbiased screening^{12,13}. The transcriptomes and epigenomes of old MuSCs have been extensively profiled^{14–23}. Despite these efforts, however, the field is still experiencing surprises, such as traditionally correlative markers that are actually causal²² and traditionally tumor-suppressive genes that promote stem cell survival and expansion²⁴. The multilayered nature of aging is also apparent in how the model of aging MuSC population dynamics varies dramatically with the assay^{16,25–28}. Thus, without comprehensive profiling of aging MuSCs, key aspects of stem cell aging may be overlooked.

Not only is too little known about aging, but there is also an inundation with extraneous correlative information⁶. Therefore, to address this knowledge gap and this knowledge excess, we took a multiomics approach to analyzing MuSC aging. Integrating multiple molecular datasets has previously been helpful in clarifying multifaceted and noisy aging systems^{5,29}. We set out to learn the unknown and to bring focus to our understanding and model of aging in these quiescent stem cells.

Results

To characterize aging at multiple levels, including those previously unprofiled in MuSCs, we generated transcriptomic, proteomic, metabolomic, and epigenomic profiles of quiescent MuSCs freshly isolated from young (4 months) and old (22 months) male C57BL/6 mice (Figure S1A). We chose transcriptomic data as sensitive and comprehensive, proteomic data as less sensitive but incorporating translational and post-translational regulation, metabolomic data as noisier but essential for disambiguating the consequences and causes of certain gene expression changes, and DNA methylation as a type of epigenomic data that is stable during MuSC isolation and linked to chronological and biological age^{30,31} (Figure S1A).

For transcriptomics, we performed RNA sequencing (RNA-seq), using as replicates MuSCs from individual mice (4 young and 4 old). We detected reads from 24,630 genes (Table S1), of which 11,167 passed the threshold for expression (at least 2 FPKM in at least one sample). Samples clustered by age (Figure 1A), and many genes were different between the two age groups – 6256 genes at an FDR of 5% (Figure 1B). Some of the top increased genes were inflammatory and senescence-associated secretory phenotype (SASP) genes (Il33, Ccl11, Mmp3, Igtp), extracellular matrix genes (Thbs4, Col4a6, Col8a1), and apoptosis genes (Perp, Sfrp4). Top decreased genes included genes important for general muscle development and function (Mest, Gamt, Popdc2), protein-folding genes (Hspa1b, Dnaja4), and genes important for MuSC function (Lix1, Ccnd1).

For proteomics, we performed shotgun mass spectrometry (MS), using as replicates pools of MuSCs from multiple animals (3 young replicates and 2 old replicates, with each replicate pooled from 16 to 20 mice). Samples clustered by age (Figure 1C). We detected peptides from 4218 genes (Table S1); 83% were expressed at the transcript level as determined by RNA-seq. There were 714 proteins that were consistently different between young and old MuSCs (Figure 1D). Top increased proteins with age were related to lipid metabolism

(Hacd3, Ces1d), lysosomal metabolism (Gns, Man2b2), and the glutathione (GSH)-mediated response to oxidative stress (Triap1, Gclc). Top decreased genes were the senescence-downregulated marker Lamb1, RNA transcription and modification genes (Ddx39, Sf3b3, Polr2a, Nsun2), and the MuSC quiescence marker Calcr.

For metabolomics, we performed mixed-phase high-performance liquid chromatography (HPLC) coupled with positive-mode electrospray ionization (ESI) and MS on methanol-extracted metabolites, using pools of MuSCs as replicates (8 young replicates and 12 old replicates, each pooled from 2 to 6 mice). Although more variable than the gene expression data, as expected, samples generally clustered by age (Figure 1E). After filtering for noise, we detected 596 features (Table S1), of which 353 mapped to a metabolite in the KEGG compound database, totaling 189 unique metabolites. At an exploratory FDR of 30%, 31 metabolites differed in abundance between young and old MuSCs (Figure 1F). Top increased metabolites were the amino acid metabolites citramalic acid and 3-hydroxyanthranilic acid, and creatinine. Top decreased metabolites were GSH and its precursors glutamate and 5-oxoproline, creatine, and uridine diphosphate (UDP) and its related metabolites.

Finally, we performed epigenomic profiling through whole-genome bisulfite sequencing (WGBS), using as replicates MuSCs from individual mice (4 young and 4 old). We profiled 115–200 million reads per sample (60–70% uniquely mapped), altogether covering 37 million CpGs (out of 42 million total in the mouse genome) in at least one sample. Samples clustered by age (Figure S1B). We used DSS to call differentially methylated CpGs (Figure 1G and Figures S1C–S1D)³², which numbered 78,375 at an FDR of 5%, and differentially methylated regions (DMRs) (Figure 1H and Table S1) which numbered 1570, 546 of which were near genes.

The distribution of MuSC DNA methylation over different aspects of the genome was similar to that previously described^{16,33–35} (Figure S1E). At these global levels in bulk populations, young and old quiescent MuSCs were extremely similar, though a recent study found that DNA methylation variability increases across cells when analyzed at a single-cell level¹⁶. We also found that DNA methylation over H3K4m3 peaks or H3K27m3 peaks in quiescent MuSCs globally did not differ by age¹⁵. As described previously for quiescent stem cells^{16,34}, with age there was an overall tendency toward hypermethylation. Nevertheless, it was interesting that H3K27m3 peaks in old MuSCs exclusively gained rather than lost DNA methylation. It is known that, away from promoters, H3K27m3 and EZH2 recruit DNMT1/3a/3b^{36–38}. However, sequential chromatin immunoprecipitation coupled with bisulfite sequencing (ChIP-BS-Seq) analyses^{36,39} and other studies of DNA methylation and H3K27 methylation^{37,40–43} have shown that when analyzed specifically at CpG island promoters, DNA hypermethylation and H3K27m3 are mutually exclusive marks in physiological situations (an exception possibly in oncogenesis). Surprisingly, when we examined the co-occurrence of DNA hypermethylation and H3K27m3 at CpG island promoters, we found that this “epigenetic mismatch” was nearly absent in young MuSCs but present in old MuSCs (Figure S1F). At a cutoff of DNA hypermethylation 90%, there are 50 occurrences in old MuSCs compared to just 1 in young MuSCs. One possible explanation for this is the existence of heterogeneity within the old MuSC population that is less present

in young MuSCs¹⁶. Together, these results warrant a cell-by-cell analysis, if not at the epigenomic level, at least in phenotypes under consideration.

We were struck by the observation that GSH synthesis enzymes were increased with aging but GSH itself was strongly depleted (Figures 1I and 1J). On further inspection, we found that many of the enzymes that use GSH to reduce oxidized proteins and lipids were also increased with age (Figures 1B and 1D). In addition, we found the DMR of *Mgst1* (microsomal glutathione S-transferase 1), an endoplasmic reticulum glutathione transferase and peroxidase, was adjacent to a known occupancy site by the oxidative stress response transcription factor NRF2 (also known as Nfe2l2)⁴⁴ (Figure S1G). This was also at a region where H3K4m3 breadth (which is associated with transcriptional consistency⁴⁵) decreased with age, where *Mgst1* DNA methylation transitions from promoter hypomethylation to gene body hypermethylation, and where *Mgst1* has alternative promoters. Although our RNA-seq data was not deep enough to reliably identify which promoters are differentially used in MuSCs, we found that the total transcript levels of *Mgst1* increased with age (Figures 1B and S1G). Altogether, these data suggest that old MuSCs have decreased GSH at the metabolite level, but have mounted an oxidative stress and GSH biosynthetic response at epigenomic, transcriptomic, and proteomic levels.

To further examine the pathways that are altered with aging across multiple levels of molecular function, we integrated our data using a pathway rank aggregation strategy. We selected the KEGG database of pathways as updated and comprehensive, spanning multiple types of data and additionally containing interaction-level data^{46,47}. We first performed individual pathway enrichment/overrepresentation analyses in each of the individual transcriptomic, proteomic, metabolomic, and epigenomic datasets (Table S2). We then had these individual datasets vote with these pathway preference lists, and we generated a consensus list based on rank aggregation optimizing the coherence between the consensus list and individual ordered lists⁴⁸ (Figure 1J and Table S2). Indeed, GSH metabolism rose to the top of the consensus list; although not at the very top of most of the individual datasets except for proteomics, it was among the top twenty across datasets (Figures S2A–S2C). An alternative method of rank aggregation based on a prioritization of rank vector significance also showed that GSH metabolism was at the top of the consensus list⁴⁹ (Table S2).

To characterize GSH metabolism in old MuSCs at a single-cell level, we employed the ThiolTracker Violet molecular probe, which allows live-cell staining of GSH content⁵⁰. After MuSC isolation and incubation with ThiolTracker, we confirmed that the overall ThiolTracker signal was diminished in old MuSCs compared to young MuSCs (Figure S2D). However, we found that the distribution of GSH content in old MuSCs, unlike in young cells, was bimodal, revealing distinct GSH^{high} and GSH^{low} populations (Figures 2A and 2B). We next assessed the levels of GSH over an age gradient. To address this, we isolated MuSCs from mice at 4, 17, 24, and 31 months of age and measured GSH content with ThiolTracker. We found that with advancing age the ratio of GSH^{high} to GSH^{low} MuSCs decreased (Figure 2C).

Old MuSCs exhibit dramatic defects in activation rate and survival^{22,24}. Therefore, we asked whether MuSC dysfunction might be heterogeneous and associated with the GSH content in

these cells. We isolated the GSH^{high} and GSH^{low} subpopulations of old MuSCs and assayed for the rate of S-phase entry (using EdU incorporation over 48 hours in culture) and for cell survival (using propidium iodide staining after 24 hours in culture). We found that the GSH^{high} subpopulation of old MuSCs activated and survived in a manner similar to young MuSCs, while the GSH^{low} population had marked defects in both S-phase entry and survival (Figures 2D–2E and Figure S2E). Additionally, cell size for GSH^{high} MuSCs grew more quickly during the activation process compared to that of their GSH^{low} counterparts (Figure S2F).

Recent work has shown that old MuSCs consume less oxygen and acquire mitochondrial defects compared to young MuSCs¹⁸. We isolated GSH^{high} and GSH^{low} old MuSCs and used the Seahorse assay to measure oxygen consumption and mitochondrial function. We found that GSH^{low} cells have decreased basal oxygen consumption, ATP-linked respiration, and maximal respiratory capacity, suggesting lower ATP demand and reduced total mitochondrial capacity in these cells (Figures 2F and S2G–S2I). Given the reported link between mitochondrial dysfunction and impaired mitochondrial autophagy (mitophagy)⁵¹, we next asked whether GSH^{low} MuSCs have lower mitophagic flux compared to GSH^{high} MuSCs. We thus measured mitophagic flux as the change in MitoTracker Green (which stains total mitochondria) before and after autophagy blockade. We observed that GSH^{low} MuSCs exhibited lower mitophagic flux compared to both GSH^{high} and young MuSCs (Figure S2J). However, we found no significant difference in the total mitochondrial content between GSH^{high} and GSH^{low} MuSCs (Figure S2K), suggesting that GSH^{low} MuSCs have lower mitochondrial turnover. Because defective mitochondrial turnover can lead to increased mitochondrial ROS, we measured mitochondrial ROS production from GSH^{high} and GSH^{low} MuSCs using the MitoSox probe. Consistent with this premise, we found that GSH^{low} MuSCs had significantly more mitochondrial ROS compared with their GSH^{high} counterparts (Figure S2L).

To address the functionality of GSH^{high} and GSH^{low} MuSCs *in vivo*, we isolated these two subpopulations of YFP-labeled old MuSCs and transplanted them into injured, irradiated muscles of 4-month-old recipient mice. Consistent with the *ex vivo* results, the GSH^{high} cells were able to contribute to *in vivo* myogenesis more effectively than the GSH^{low} cells (Figure 2G) as measured by an increase in the number of YFP+ muscle fibers. Taken together, our results suggest that old MuSCs form a bimodal GSH distribution, with the GSH^{high} population exhibiting more youthful characteristics than the GSH^{low} population.

The pool of GSH is primarily maintained by (1) *de novo* synthesis, which can be experimentally augmented by supplying a cysteine precursor, N-acetylcysteine (NAC), and (2) recycling of oxidized glutathione using NADPH generated largely through the pentose phosphate pathway⁵², which can be experimentally prevented by the G6pd inhibitor 6-aminonicotinamide⁵³ (6-AN) (Figure S3A). These tools allowed us to test whether GSH levels were causal or correlative regarding MuSC function.

We first addressed this question in old MuSCs. We separated GSH^{high} and GSH^{low} old MuSCs and provided NAC to GSH^{low} cells. We found that replenishing GSH in GSH^{low} MuSCs rescued the rate of S-phase entry and survival (Figures 3A–C). To confirm that

these functional improvements in response to NAC were specific to GSH replenishment (i.e., the result of direct conversion of NAC into GSH), we inhibited glutamate-cysteine ligase (Figure S3A), the rate-limiting enzyme of GSH synthesis, using buthionine sulfoximine (BSO)⁵⁴. In the presence of BSO, NAC was unable to rescue the function of GSH^{low} old MuSCs (Figures 3A–C).

We next investigated the consequences of decreasing GSH levels in young MuSCs. In response to GSH depletion through 6-AN treatment, young cells activated at rates similar to the GSH^{low} population of old cells (Figure 3D). This could be rescued by supplying NAC (Figure 3D). In all of these ex vivo experiments, we used ThiolTracker to confirm that the changes in GSH levels caused by NAC, BSO, and 6-AN were within the physiological ranges observed in young and old MuSCs and represented changes in the population at large rather than in just a few cells (Figures 3E and S3B). In total, these experiments show that GSH is central to MuSC survival and efficient progression to S-phase during activation.

Next, we tested the effects of NAC treatment on GSH levels and MuSC function in vivo in old mice. We found that intramuscular NAC injections elevated the GSH content of old MuSCs after injury (Figure S3C). These intramuscular NAC injections rescued the rate of S-phase entry in vivo (Figure 3F). Taken together, these results highlight the necessity and sufficiency of intracellular GSH levels for maintaining the function of MuSCs, both ex vivo and in vivo.

To address the potential for NAC supplementation to improve old muscle regeneration, we treated 28-month-old mice with NAC or vehicle in the drinking water for 2 weeks, at which point we injured tibialis anterior (TA) muscles with barium chloride. We found that muscle regeneration, as measured by regenerating myofiber cross sectional area (CSA) 7 days after injury, was dramatically improved in NAC-supplemented mice (Figure 3G and S3D).

Next we asked if depleting GSH content in young mice could impair the regeneration of young muscle. Young mice were treated with BSO in the drinking water for 2 weeks, at which point we injured the TA muscle with barium chloride. Consistent with a decrease in GSH content from the MuSCs isolated from these mice (Figure S3E), we found that muscle regeneration was significantly impaired in these mice. (Figure S3F).

To explore the mechanisms underlying the bimodality in GSH content in old MuSCs, as well as what might be contributing to the role of GSH in mediating MuSC function, we performed transcriptomic analysis of young MuSCs, GSH^{high} old MuSCs, and GSH^{low} old MuSCs (Table S3). Consistent with the phenotypic differences, we found that by principal component analysis (PCA), the GSH^{high} old cells were overall more transcriptionally like young cells than were their GSH^{low} counterparts (Figure 4A). Specifically, GSH^{high} cells were more youthful with respect to pathways such as cell cycle and inflammation (Figure 4B).

However, we noticed that, with respect to the second principal component, GSH^{low} old MuSCs displayed a more youthful signature compared to their GSH^{high} counterparts (Figure 4A). When we explored which pathways contribute most to this principal component, we found, quite unexpectedly, that GSH metabolism was strongly enriched (Figure 4C). This

left us with the following conundrum: why are GSH^{low} old cells transcriptionally more similar to young cells with respect to GSH metabolism? We examined the specific genes driving this signature, and we observed that GSH^{high} cells, compared to GSH^{low} cells and young cells, displayed higher levels of genes involved in GSH biosynthesis, including genes involved in the de novo synthesis of GSH and genes involved in generating the reducing power needed for GSH replenishment. We confirmed this result with RT-qPCR using samples independent of those used in the RNA-Seq (Figures 4D and S4A). We also confirmed these differences at the protein level by performing western blots for these GSH biosynthetic enzymes in GSH^{high} and GSH^{low} populations (Figure 4E and Supplemental Figure S4B). Taken together, these results led us to the following new view of MuSC aging: GSH^{high} cells are able to upregulate GSH biosynthetic and metabolic genes to maintain GSH levels, while GSH^{low} cells lack a compensatory response to GSH depletion. Young cells likely have no need to engage these pathways because of high GSH levels and thus appear transcriptionally similar to the uncompensated GSH^{low} subpopulation of old cells with respect to GSH metabolism. Furthermore, our data suggests that the compensatory signature in the multiomics analysis is a signature driven by a subset of the old MuSCs (the GSH^{high} old cells). By extension, perhaps the decrease in GSH content in our metabolomics analysis is also driven by a different subset (the GSH^{low} old cells).

To understand why only a portion of the old MuSCs are able to engage the compensatory upregulation of GSH biosynthetic genes, we used GSEA to examine which transcription factor target gene signatures⁵⁵ are enriched in GSH^{high} or GSH^{low} MuSCs. We found that the top transcription factor with targets enriched in GSH^{high} MuSCs was the oxidative stress response factor NRF2 (Figure 4F). Transcription factors with targets enriched in GSH^{low} MuSCs included the pro-aging transcription factors NF- κ B and Smad3 (Figure 4G)^{22,56-58}. Indeed, upon inspection, we identified a binding site for NRF2 in the promoters of nearly all the genes involved in the compensatory GSH metabolic signature. In addition to GSH biosynthetic genes, our transcriptomic analysis revealed changes in many of the other canonical NRF2 target genes, as well as robust changes in many of the well-established NF- κ B targets (Figures S4C and S4D).

Because of the NF- κ B signature in GSH^{low} MuSCs, and because NRF2 and NF- κ B can be mutually antagonistic⁵⁹, we hypothesized that aberrant NF- κ B signaling in the GSH^{low} cells inhibits NRF2 transcriptional activity, resulting in the lower levels of GSH biosynthetic enzymes and GSH content in these cells. Prior work has shown that genetic activation of NF- κ B in MuSCs does not affect cell number or clone formation ability⁶⁰, and that NF- κ B activity is important for activated MuSC proliferation and survival⁶¹, but the effects of NF- κ B inhibition on quiescent old MuSCs in terms of the readiness of these cells to exit quiescence has not been tested. Therefore, we treated old mice with either vehicle control or the NF- κ B inhibitor JSH-23⁶². The inhibitor was administered by intraperitoneal injection for 5 days followed by MuSC isolation on the sixth day. Compared to vehicle control, JSH-23 led to increased S-phase entry and cell survival during exit from quiescence of old MuSCs (Figures 4H and 4I). Importantly, we also observed an increased ratio of GSH^{high} to GSH^{low} MuSCs after JSH-23 treatment compared to control treatment (Figure 4J), consistent with idea that NF- κ B downregulates GSH levels in quiescent MuSCs. To confirm these finding using an orthogonal molecular genetic approach, we treated old mice

with either an antisense morpholino (AMO) against the NF- κ B subunit RelA/p65 or a control AMO for 1 week. Consistent with the pharmacological data, MuSCs isolated from old mice treated with a RelA AMO exhibited decreased NF- κ B target gene expression, increased NRF2 target gene expression, and increased GSH content (Figures 5A, 5B, S5A, and S5B).

Previous work from our lab and others has shown that the aged environment can contribute to the aging-associated decline in stem cell function^{63,64}. Therefore, we asked if young mice exposed to an old environment might exhibit increased NF- κ B activity and decreased GSH content. To address this experimentally, we injected young mice with serum from old mice or, as the control, with serum from young mice (0.3 mL daily for 3 days) and isolated MuSCs for analysis the following day. We found that MuSCs from young mice that had received old serum had increased expression of canonical NF- κ B target genes and an increase in the GSH^{low} population of MuSCs compared with controls (Figures 5C and S5C–S5D).

Collectively, our data suggest a stressor-response model of quiescent MuSC aging. Young MuSCs are exposed to relatively low levels of oxidative stress and therefore show minimal signs of an oxidative stress response. These cells are GSH-replete and function well. Old MuSCs are exposed to oxidative stress and respond in one of two ways. Old GSH^{high} MuSCs mount a compensatory response by upregulating NRF2 transcriptional activity and GSH synthesis. These cells are GSH-replete and maintain function in the face of the stressors of aging. On the other hand, old GSH^{low} MuSCs decompensate due to maladaptive NF- κ B activation that inhibits NRF2 activity, represses the GSH synthesis machinery, and thereby leads to dysfunction. The functionality of these GSH^{low} cells can be rescued by replenishing GSH exogenously. Thus, our work reveals the power of multiomics to uncover previously cryptic heterogeneity and complex feedback loops during aging. Furthermore, we have elucidated a heretofore unrecognized cause of aging-associated cellular dysfunction, namely the lack of compensation in the face of aging-associated stress.

Discussion

Using a multiomics approach, we have shown that GSH metabolism is the most significantly altered pathway across the epigenome, transcriptome, proteome, and metabolome in old MuSCs. While GSH itself is the most significantly depleted metabolite with age, an apparent compensatory signature of upregulation of the genes and proteins responsible for GSH biosynthesis. At first glance, the decrease in GSH and the increase in the GSH biosynthetic response appeared to be an example of incomplete compensation. However, the data suggest a model that is markedly different from this original hypothesis of incomplete compensation. Using a single-cell ThiolTracker-based approach, we have shown that old MuSCs exhibit a bimodal distribution in GSH content. While approximately half of old MuSCs display levels of GSH that are comparable to those in young MuSCs, the other half exhibit a dramatic depletion of GSH. Upon further analysis of these distinct populations of old MuSCs, we identified a strong NRF2-associated compensatory response in the GSH^{high} population and the lack of such a response in the GSH^{low} population. Finally, we have shown that

pharmacological or genetic inhibition of NF- κ B, a known antagonist of NRF2, rescues both the functionality as well as the GSH^{high}-to-GSH^{low} ratio of old MuSCs.

While other studies have applied individual or a few select omics techniques to characterize the molecular changes of aging^{15–17}, our work employs a broader multiomics approach. Profiling data yields correlative changes (without functional consequences), causal changes (that directly create phenotype), and compensatory changes (that preserve phenotype). Studying compensatory changes may be as important as studying causal changes in understanding aging, and in designing therapeutic strategies it is clearly important to discriminate between the two. By utilizing a multiomics approach, in particular by incorporating direct metabolic data, we were able to identify a compensatory signature surrounding glutathione metabolism by noticing an apparent contradiction between what we observed at the level of the metabolome and what we observed at the level of the epigenome, transcriptome, and proteome.

Our data supports the following model for the dichotomous response to oxidative stress by old MuSCs: GSH^{high} MuSCs have upregulated NRF2 activity, increasing both GSH utilization and synthesis, reducing oxidative stress and maintaining GSH levels. GSH^{low} MuSCs have instead upregulated activity of the pro-aging transcription factors NF- κ B and Smad3, increasing inflammation and impairing activation ability, all the while failing to maintain GSH levels. Mutual antagonism can lead to such bistable states^{65,66}. As NRF2 and NF- κ B, as well as NRF2 and Smad3, are mutually antagonistic^{59,67}, these transcription factors may form the basis of the two GSH-defined states of old MuSCs.

One finding that remains enigmatic is that some MuSCs adopt the NRF2-dominant, GSH^{high} state and other MuSCs adopt the NF- κ B/Smad3-dominant, GSH^{low} state in response to aging or exposure to aged serum. MuSCs experience heterogeneous proliferative histories and environmental exposures. For example, spontaneous exit from quiescence, which occurs more for some MuSCs than others during aging²⁸, may increase NRF2 activity due to the oxidative demands of proliferation and the role of NRF2 in proliferation⁶⁸. In addition, quiescent MuSCs are heterogeneous in proximity to capillaries^{69,70}, and one would also expect there to be heterogeneity in interactions with other cell types such as macrophages, fibroblasts, and fibroadipogenic progenitors, all of which would affect early exposure to pro/anti-inflammatory cytokines, growth/stasis factors, and oxygen/nutrient stress and predispose MuSCs to adopting one of the two states during aging^{71–73}. Thus, molecular feedback loops may consolidate heterogeneous exposures into relatively stable discrete states during aging.

Despite this proposed stability of the two states, however, we observed some degree of plasticity in that the fraction of GSH^{low} MuSCs: GSH depletion, aged serum, or aging itself increases the GSH^{low} fraction, and either NAC or NF- κ B inhibition converts GSH^{low} MuSCs into GSH^{high} MuSCs. While the present study focuses on aging, MuSC function is also disrupted in other states such as muscular dystrophy⁷⁴, and it would be interesting to study GSH^{high}/GSH^{low} states and NAC in MuSCs in these diseases. Regarding aging, others have observed a depletion of GSH with age in many diverse tissue types⁷⁵, and here we have shown that GSH levels are crucial for proper function of MuSCs during activation, and

that the depletion of GSH in a subset of MuSCs during aging can, in large part, explain the defects observed in these old MuSCs. This has important implications for developing treatments and preventions for MuSC dysfunction during aging, and for understanding how interventions that affect redox signaling and inflammation, such as diet, exercise, systemic diseases, and medications, affect old MuSC function.

Limitations of Study

Although the current study used pharmacological inhibitors and morpholino treatment to discern the role of NF- κ B signaling in driving the emergence of GSH bimodality, a MuSC-specific NF- κ B KO mouse model would help avoid the potential for confounding systemics affects. The current study would also benefit from a complete multiomic analysis of the GSH high and low sub populations to quantify exactly the extent to which the bulk sequencing results could be segregated by the individual contribution from GSH^{high} and GSH^{low} MuSCs. Additionally, the current study could benefit from muscle function assessment data, including force production and gait analysis, to complement the muscle fiber regeneration data. Finally, we have yet to uncover the ultimate upstream driver for the emergence of GSH bimodality with age, and future studies may build upon the present work by identifying the ultimate cause of GSH bimodality with age.

STAR METHODS

RESOURCE AVAILABILITY

- Metabolomics data have been deposited to the EMBL-EBI MetaboLights database⁷⁶ with the identifier MTBLS1779. Sequencing data have been deposited in NCBI's Gene Expression Omnibus (GEO)⁷⁷ with accession number GSE152798.
- Raw data used to generate graphs and western blots are included in Data S1 and Data S2.
- This paper does not report original code.
- Any additional information required to reanalyze the data reported in this paper is available from the lead contact upon request

Lead contact—Further information and requests for resources and reagents should be directed to and will be fulfilled by the lead contact, Thomas Rando (rando@stanford.edu)

Materials availability—This study did not generate new unique reagents

EXPERIMENTAL MODEL AND SUBJECT DETAILS

Animals—Animals were housed and maintained in the Veterinary Medical Unit at the Veterans Affairs Palo Alto Health Care System. Animal protocols were approved by the Institutional Animal Care and Use Committee. Young mice used in these studies were 4 months old; old mice were either 17, 24 or 31 months old, as indicated. Young C57BL6 mice were purchased from The Jackson Laboratory (000664). Old C57BL6

mice were obtained from Charles River Laboratories through the National Institute on Aging. NSG mice were purchased from The Jackson Laboratory (005557). *Pax7^{CreER/+}*; *ROSA26^{YFP}* mice were obtained by crossbreeding *Pax7^{CreER}* mice on the C57BL/6 × 129/SvJ background (Dr. Charles Keller at Oregon Health & Science University) with *ROSA26^{YFP}* (006148) mice purchased from The Jackson Laboratory (006148).

Drug Treatments—The inducible CreER recombinase system was activated by injecting Tamoxifen (Sigma-Aldrich) at a dose of 20 mg/mL in corn oil. Mice received 2 mg Tamoxifen intraperitoneally daily for seven consecutive days. NAC was dissolved in PBS and administered via intramuscular injection 24 and 48 hours post-injury at a dose of 150 mg/kg. For control mice, injections consisted of PBS only. For the JSH-23 studies, JSH-23 was dissolved in DMSO and administered at a dose of 1.5 mg/kg. For control mice, injections consisted of DMSO only.

Muscle Injury—For muscle injuries, mice were anesthetized with isoflurane before TA muscles were disinfected with ethanol and iodopovidone, injected with 50 µl BaCl₂ (Sigma), and poked 50 times with a 31-gauge needle. Mice received post-surgery buprenorphine analgesia.

METHODS DETAILS

MuSC isolation—MuSC isolation by FACS was performed as previously described. Briefly, hindlimb muscle was dissected and homogenized manually with dissection tools before incubation with type II collagenase and dispase digestive enzymes. Following enzymatic digestion, samples were mechanically dissociated using a 20G needle and syringe. Cells were then filtered through a 40 µm cell strainer. The bulk tissue prep was incubated with fluorescently labeled antibodies at 4°C for 1 hour before a subsequent filtering step through a 35 µm strainer and MuSC isolation by FACS. MuSCs were purified from bulk tissue prep by positive selection for cells expressing VCAM and negative selection against cells expressing CD45, CD31, and Sca1.

RNA-Seq transcriptomics—For the initial aging transcriptomics, quiescent MuSCs were purified by FACS, washed with cold PBS, snap-frozen in liquid nitrogen, and stored at –80°C until analysis. RNA was extracted with the Nucleospin RNA XS kit (Machery-Nagel), including DNase treatment. The ERCC RNA Spike-in Mix (ThermoFisher) was added proportional to cell number as part of a larger experimental design involving different cell types; reads aligning to ERCC RNA were subsequently removed from analysis. RNA (10 ng) was reverse-transcribed using oligo(dT) priming and linearly amplified with the SMARTer Ultra Low Input system (Takara). The cDNA was then sheared with a Covaris S2 ultrasonicator. End repair, multiplexed adaptor ligation, and 6–9 cycles of library amplification were performed using the Ovation Ultralow multiplex system (NuGEN). Libraries underwent paired-end 101-bp sequencing at the Stanford Genome Sequencing Service Center with an Illumina HiSeq 2000 to a depth of 26–37 million reads.

Reads were adapter- and quality-trimmed with trim_galore (www.bioinformatics.babraham.ac.uk/projects/trim_galore). Trimmed reads were mapped

to mm10 using transcript annotations from Ensembl with STAR⁷⁸ (multimap filter 10, mismatches filter 10 with length fraction 0.4, minimum intron 20 bp, maximum intron 500,000 bp). Exonic reads that mapped uniquely were summarized over genes with the featureCounts module of the Subread package⁷⁹. Raw counts were analyzed using edgeR⁸⁰ (normalization method TMM, differential expression testing with Cox–Reid estimations of tagwise dispersions and the negative binomial GLM likelihood ratio test). Multiple hypothesis testing was corrected with the Benjamini-Hochberg method. Only genes with Entrez identifiers were used, and downstream analyses included only genes with at least 2 fragments per kilobase million (FPKM) in at least 1 sample.

Shotgun proteomics—Shotgun proteomic samples were prepared by precipitating MuSC proteomes using 100% TCA (Sigma), which was added to yield a final concentration of 20%. Samples were incubated at -80°C overnight to precipitate proteins and then centrifuged at 4°C for 10 minutes at 10,000*g*. The pellet was washed 3 times with ice cold 0.1 M HCl in 90% acetone, air-dried, and then resuspended in 30 μL 8M urea in PBS. ProteaseMAX (30 μL of 0.2% in 100 mM ammonium bicarbonate) was then added to samples, after which the samples were vortexed and diluted with 40 μL ammonium bicarbonate. TCEP was added to a final concentration of 10 mM and then samples were incubated for 30 minutes at 60°C , followed by addition of iodoacetamide to a final concentration of 12.5 mM, and samples were incubated at room temp for 30 minutes. Samples were diluted with 100 μL of PBS and 1.2 μL of 1% ProteaseMAX was added and vortexed well, after which 2 μg of sequencing trypsin was added and samples incubated overnight at 37°C . Trypsinized samples were acidified with 5% formic acid and centrifuged at 13,200 rpm for 30 minutes.

Purified peptides were pressure-loaded onto a 250 mm silica capillary tubing filled with 4 cm of Aqua C18 reverse-phase resin (Phenomenex #04A-4299). The samples were then attached using a MicroTee PEEK 360 μm fitting (Thermo Fisher Scientific #p-888) to a 10 cm laser pulled column of 100 mm fused silica capillary packed with 10 cm Aqua C18 reverse-phase resin. Samples were subsequently analyzed using an Orbitrap Q Exactive Plus mass spectrometer (ThermoFisher). Data was collected in data-dependent acquisition mode with dynamic exclusion enabled (60 seconds). One full MS (MS1) scan (400–1800 *m/z*) was followed by 15 MS2 scans (ITMS) of the *n*th most abundant ions. Heated capillary temperature was set to 200°C and the nanospray voltage was set to 2.75 kV. The samples were run using a two-hour gradient from 5% to 80% acetonitrile with 0.1% formic acid at 100 nL/minute. Data were extracted in the form of MS1 and MS2 files using Raw Extractor 1.9.9.2 (Scripps Research Institute) and searched against the Uniprot mouse database using ProLuCID search methodology in IP2 v.3 (Integrated Proteomics Applications, Inc)⁸¹.

Peptide counts were normalized to total spectral counts for each sample. Protein identifiers were converted to Entrez gene identifiers for subsequent analysis. Proteins were considered reliably changed with age if the expression in all old samples was greater than that in all young samples or vice versa, equivalent to a Mann-Whitney two-tailed *u*-test value of 0.2.

LC-MS metabolomics—For the aging metabolomics, quiescent MuSCs were purified by FACS. MuSCs were triple-counted with a hemocytometer, gently washed 3 times with cold

PBS, snap-frozen in liquid nitrogen, and stored at -80°C . Pellets were extracted with 80% methanol at 3 million cells/mL. Samples were vortexed vigorously for 1 minute, incubated at 4°C for 15 minutes, and then centrifuged at $21,000g$ for 15 minutes at 4°C . 150 μL of supernatant was transferred to glass vials and stored at -80°C until analysis. Samples were analyzed as described⁸². Briefly, extracts were analyzed using mixed-mode columns (ODP2 HP-4B, Shodex). Chromatography was performed with a mobile-phase gradient of 10% to 90% acetonitrile in 10 mM ammonium acetate, at 0.1 mL/min for 30 minutes, with subsequent modification with 10 mM acetic acid for positive ionization. Samples were then analyzed on a Waters UPLC-coupled Exactive Orbitrap mass spectrometer (ThermoFisher). Mass spectrometry acquisition was performed in profiling positive electrospray ionization mode over 75–1200 m/z with scans captured every 0.5 seconds at 100,000 mass resolution.

Raw data were centroided using PAVA⁸³. Peaks were extracted using XCMS⁸⁴ (method centWave, maximum consecutive m/z deviation 3 ppm, minimum m/z difference for overlapping retention times 0.0005, trace filter at least 3 peaks with intensity 100, peak width 10–60 seconds, signal-to-noise threshold 3, no Gaussian fit, integration on Mexican hat filtered data, m/z center function weighted mean). Features were batch-corrected for retention time using SIMA (retention time threshold 150 seconds, m/z threshold 0.006) and intensity values using ComBat^{85,86}. Features were mapped to the Human Metabolome Database based on hydrogen, ammonium, sodium, and potassium adducts with a mass tolerance of 0.000005, and then identifiers were converted to those in the KEGG Compound database^{87,88}. Rank products were used to generate a list of metabolites that differ with age with an exploratory FDR of 30%⁸⁹.

WGBS DNA methylomics—For the aging epigenomics, quiescent MuSCs were purified by FACS. MuSCs were snap-frozen, and genomic DNA was extracted with the QIAamp DNA Micro kit (Qiagen). Bisulfite sequencing libraries were generated using a method developed for low sample input. DNA (150 ng) was sheared with a Bioruptor 300 (Diagenode) and then end-repaired and A-tailed with the NEBNext DNA Library Prep Master Mix (NEB). Methylated Illumina adapters were ligated using LigaFast (Promega), and size selection was performed with AMPure XP beads (Beckman Coulter). Bisulfite conversion was performed with the EZ DNA Methylation Direct kit (Zymo) and amplified for 14 cycles with PfuTurbo Cx Hotstart DNA Polymerase (Agilent) followed by final size selection with the AMPure XP beads. Libraries underwent paired-end 101-bp sequencing with added PhiX spike-in control at low cluster density to a depth of 115–200 million reads.

Reads were adapter- and quality-trimmed with trim_galore (quality cutoff 20, adapter stringency 1, final length filter 50) and then deduplicated, mapped to the mm10 version of the mouse genome, and called for methylation using Bismark⁹⁰ (seed mismatches 1, max insertion 1000 bp, omit from the second read 2 bp). Bisulfite conversion efficiency (as assessed by conversion of non-CpG cytosines) was $>99.5\%$. DSS was used to estimate methylation level means and dispersions with local smoothing (span 500 bp), to test individual CpGs for statistical significance (Wald test of the beta-binomial distribution³²; multiple hypothesis testing correction with the Benjamini-Hochberg method), and to identify DMRs (p-value threshold 0.005, minimum CpGs 3, minimum length 4, minimum significant fraction 0.9). For pathway analysis, the foreground set of genes were all KEGG genes

with a DMR within 500 kb upstream of the transcription start site (TSS) to the end of the transcription end site (TES). The background set of genes was generated by rerunning this analysis with the p-value threshold set to 1, thus listing all possible genes that could potentially have a DMR given the CpGs profiled (which was 22,385 out of 22,603 total KEGG genes).

To analyze DNA methylation over regions, CpG islands were obtained from the UCSC Table Browser^{91,92}. CpG island shores were defined as the 2 kb upstream and downstream of a CpG island that was not at another CpG island⁹³. HCPs, ICPs, and LCPs were defined as previously³⁵, and were generated with compEpiTools in R⁹⁴. Gene bodies were defined as 3000 bp downstream of the TSS of GENCODE genes to the TES⁹⁵. Intergenic was considered 10 kb away from any transcript-encoding region. H3K4m3 and H3K27m3 peaks were published previously and were acquired from GEO at accession GSE47362^{15,77}. NRF2 peaks were published previously and were acquired from GEO at accession GSE72964⁴⁴. H3K27m3 peaks in proximity to CpG island promoters were defined as peaks overlapping a region 5 kb upstream to 1 kb downstream of the TSS of GENCODE genes where there was also a CpG island.

Pathway analysis—Custom code (R package “multiomics,” available at the link below) was used to integrate multiple types of molecular data, automating data deduplication, identifier conversion, different types of pathway enrichment and overrepresentation analysis, and rank aggregation. For the present study, KEGG Pathways were used⁴⁶. For RNA-Seq transcriptomics and shotgun proteomics data, GSEA was done using p=1 weighting of the absolute Signal2Noise ratio metric, and scoring used gene permutation testing⁹⁶. For LC-MS metabolomics and WGBS DNA methylomics data, overrepresentation analysis was done using Fisher’s exact test (one-tailed for enrichment) with the Benjamini-Hochberg correction for multiple hypothesis testing. For genes, all pathways containing 30 to 200 profiled genes were used; for metabolites, all pathways containing 3 to 200 profiled metabolites were used. Euler diagrams were produced with the eulerr package in R. Ranks were aggregated with the R packages RankAggreg for coherence-based aggregation and RobustRankAggreg for probabilistic-based aggregation^{48,49}. For coherence-based aggregation, the Cross-Entropy Monte Carlo algorithm was used to optimize the Spearman footrule distance metric, and 80 pathways were requested for return (more was computationally not feasible); defaults were used for the other parameters. Pathways that were not assessed by a dataset (due to failing cutoffs for the number of elements profiled) were considered at the bottom of the list for coherence-based aggregation. For both methods, pathways were ranked in individual lists by p-values of the enrichment or overrepresentation analysis. The rhoScores function of RobustRankAggregation was used to calculate the exact p-value of the rank vector.

As an alternative method or rank aggregation based on prioritization of rank vector significance rather than rank coherence, we used PaintOmics 3^{97,98}. We analyzed all four input dataset types with the following cutoffs to generate foreground and background sets: RNA-Seq transcriptomics at FDR 0.2%, shotgun proteomics at Mann-Whitney u-test p-value 0.2, metabolomics as for the multiomics package above, and WGBS DNA methylomics as for the multiomics package above. The Fisher combined probability test was used to rank the final list and corrected for multiple hypothesis testing with the Benjamini-Hochberg

method. For the pathways interaction network, pathways were displayed if the combined p-value was less than 0.1 and were connected based on linked biological processes.

Glutathione-based RNA-Seq transcriptomics—To analyze MuSC transcriptomes based on glutathione status, MuSCs were sorted by FACS from 1–2 mice. MuSCs were immediately stained with ThiolTracker Violet for 20 minutes (5 μ M, ThermoFisher) and resorted by FACS. For young MuSCs, all cells were re-collected (almost all are GSH^{high}). For old MuSCs, the population was split into GSH^{high} and GSH^{low} collection groups. RNA-Seq libraries were constructed and sequenced with the Stanford Genome Sequencing Center based on standard sequencing center oligo(dT) priming, end repair, multiplexed adapter ligation, and library amplification. Libraries underwent single-end 150-bp sequencing on a NextSeq 500 in high-output mode to a depth of 68–98 million reads. Read files were then analyzed as for the aging transcriptomics above.

Multomics software availability—Software is available at <https://github.com/jamieobrett/multomics>.

Multomics data availability—Metabolomics data have been deposited to the EMBL-EBI MetaboLights database⁷⁶ with the identifier MTBLS1779.

Sequencing data have been deposited in NCBI's Gene Expression Omnibus (GEO)⁷⁷ with accession number GSE152798.

MuSC Flow Cytometry Analysis—To measure intracellular GSH content, freshly isolated MuSCs were incubated with 5 μ M ThiolTracker Violet (ThermoFisher) for 20 minutes and analyzed in the AmCyan channel. To measure mitochondrial content, MuSCs were incubated in 300 nM Mitotracker Green FM (Invitrogen M-7514) in wash media at 37°C for 45 minutes. Mitochondrial content of each sample was recorded as mean fluorescence intensity in the FITC channel. To measure mitochondrial ROS, MuSCs were incubated in 1 μ M MitoSOX Red (ThermoFisher) in wash media at 37°C for 45 minutes. MitoSOX content of each sample was recorded as mean fluorescence intensity in the Alexa594 channel. To measure mitophagic flux, freshly isolated MuSCs were treated with 1mM chloroquine (Sigma) or vehicle for 2 hours, at which point cells were stained with MitoTracker Green FM and mitochondrial content was measured as described above.

MuSC culture—Freshly isolated MuSCs were plated in wells that were precoated with poly-D-lysine (0.1 mg/mL, EMD Millipore) and ECM (25 μ g/mL, Sigma). Cells were cultured in growth medium (GM: Ham's F-10, 20% FBS, 2.5 ng/mL bFGF, 100 U/mL penicillin, and 100 μ g/mL streptomycin). To isolate cultured MuSCs for analyses, cells were treated with trypsin and then pelleted by centrifugation at 1000g for 5 minutes. 6-AN (Cayman Chemicals) was dissolved in DMSO, stored at –20°C, and used at a final concentration of 10 μ M. NAC (Sigma-Aldrich) and BSO (Sigma-Aldrich) were dissolved in sterile PBS and were used at final concentrations of 2 mM and 1 mM respectively.

Cell transplantation—At 3 months of age, *Pax7^{CreER};R26R^{YFP}* mice received tamoxifen (80 mg per kg (body weight) in 100% corn oil via i.p. injection daily for 7 days to

label MuSCs with YFP. Mice were then aged until their use as MuSC donors. Freshly isolated YFP-positive MuSCs from 24-month-old donors were treated with ThiolTracker as described, and the GSH^{high} and GSH^{low} population of cells were re-sorted by FACS. Recipient NSG mice were prepared for transplantation with 1800 cGy of irradiation to the lower hindlimbs while under ketamine anesthesia followed by BaCl₂ injury to the TA muscles, as described above, 3 days prior to transplantation. 10,000 freshly isolated YFP-positive GSH^{high} or GSH^{low} MuSCs were pelleted and resuspended in 30 μ l PBS. Resuspended cells were injected into the TA muscles of recipient mice that were under isoflurane anesthesia. 28 days after transplantation, TA muscles were collected for analysis.

Muscle histology—To test for MuSC regenerative ability in transplantation assays, muscles were fixed with 0.5% formaldehyde for several hours, dehydrated with 20% sucrose and frozen. Transverse 7 μ m sections were generated and stained for laminin using a rat anti-laminin α 1 antibody (1:1,000, EMD Millipore MAB1903) and for YFP using a rabbit anti-GFP antibody (10 μ g/mL, Thermo Fisher A11122). DAPI was used to visualize nuclei. For each muscle, ten sections, collected at evenly spaced intervals along the rostral-caudal axis of the muscle, were analyzed in a blinded fashion for YFP-positive fiber area and number in Volocity software (PerkinElmer).

To assess myofiber cross-sectional area after either NAC or BSO treatment, muscles were frozen immediately after dissection. Cryopreserved TA muscles were sectioned at the belly of the muscle into 10 μ m sections. Sections were then fixed in 2% PFA at room temperature for 10 minutes before staining. Sections were stained and imaged on a Zeiss Observer Z1 fluorescent microscope equipped with a Hamamatsu Orca-ER camera. Regenerating central nucleated muscle fiber size was quantified using the contour functions (findContours, contourArea, and arcLength) of the open-source Python package, OpenCV (<https://pypi.org/project/opencv-python/>)

S-phase entry—To assess S-phase entry of MuSCs exiting quiescence in culture, FACS-isolated MuSCs were plated with 10 μ M EdU (ThermoFisher). After 2 days, cells were fixed and stained with the Click-iT EdU Imaging Kit (ThermoFisher) and DAPI. The fraction of EdU-positive cells was determined automatically with Volocity software. To assess S-phase entry of MuSCs after injury in vivo, lower hindlimb muscles were injured as described above, and 1.5 days later, mice received 50 mg per kg (body weight) EdU via i.p. injection. After another 12 hours, MuSCs were FACS-isolated and fixed 2 hours after plating. Cells were then stained and quantified as described above.

Seahorse assay—MuSC oxygen consumption rate (OCR) was determined using a Seahorse XFp analyzer (Agilent). Cells were FACS-isolated as described, plated in an ECM-coated 96-well Seahorse plate at 200,000 cells per well, and analyzed in Seahorse base medium (Agilent 103335-100 supplemented with 25 mM glucose, 2 mM glutamine, and 1 mM sodium pyruvate) 1 hour after plating. OCR was monitored at the basal state and after the sequential injections of the mitochondrial electron transport chain inhibitors oligomycin (3 μ M), FCCP (6 μ M), and rotenone/antimycin (2.5 μ M each)⁹⁹.

Western Blotting—GSH^{high} and GSH^{low} MuSCs were isolated from the lower hindlimb muscles of 25–27 month old mice. Cells were pooled into pellets of 200,000 cells, with cells from 4–5 specimens in each pellet. Protein from each pellet was extracted in 100 μ l of 2% SDS, 100 mM Tris, pH 7.4. Protein extracts were electrophoresed on a 4%–15% gradient polyacrylamide gel and then transferred to a PVDF membrane. The intensities of protein bands and background intensities were quantified by densitometry using ImageJ.

RT-qPCR—Cells were rinsed in PBS and then lysed. RNA was isolated using the RNeasy Mini Kit (QIAGEN) according to the manufacturer's protocol. Total RNA (0.5–1.5 mg) was reverse-transcribed using the High Capacity cDNA Reverse Transcription Kit (Invitrogen). Quantitative PCR was performed on an ABI 7900HT Fast Real-Time PCR system using custom synthesized oligonucleotide primers (Invitrogen) designed to amplify the cDNA of selected target genes. Relative quantification of gene expression normalized to GAPDH was carried-out using the comparative CT method¹⁰⁰. Each measurement was performed in triplicate.

***In vivo* knockdowns**—*In vivo* knockdowns were performed as described previously¹⁰¹. Briefly, the translation start site in the mouse RelA mRNA was identified using RelA sequences obtained from Ensembl and AceView (NCBI). An antisense vivo-morpholino was designed complementary to the sequence surrounding the translation start site of RelA (aacagatcgctccatggcagggtcc). This RelA vivo-morpholino, and a non-target control vivo-morpholino (ggttacaatctaagatcaaacgacg), were synthesized by GeneTools and dissolved in sterile PBS at 0.25 mM concentration. Mice were injected on day 1 and day 4 with 100 μ L vivo-morpholino (~25 nmol or 12.5/kg per injection) and MuSCs were isolated on day 7. To assess gene expression, a portion of MuSCs was spun down for RNA extraction followed by RT-PCR. The remained of the cells was used for ThiolTracker staining.

Serum transfers.—Serum was isolated from young (4 months of age) and old (27 months of age) mice via post-mortem cardiac puncture and stored at -80°C until use. Recipient mice were all young mice and were injected via tail with 0.3 mL serum daily for three days before analysis on the fourth day.

Statistical analysis—Unless otherwise stated, significance was calculated using two-tailed, unpaired Student's t-tests. Statistical significance for competitive transplantation was calculated using a two-tailed paired Student's t-test for relative fold change. Differences were considered statistically significant at the $p < 0.05$ level (* $p < 0.05$, ** $p < 0.01$, *** $p < 0.001$, NS: not significant). Unless otherwise noted, all error bars represent SEM. Sample size for each experiment is indicated in the corresponding figure legend.

Supplementary Material

Refer to Web version on PubMed Central for supplementary material.

Acknowledgments

We thank B. Bilen, J. T. Rodgers, B. Benayoun, L. Liu, S. A. Baker, S. Mahmoudi, and Z. Weng for helpful discussions on approach and analysis, and S. Seisenberger and D. Wenemoser for sharing valuable technical expertise.

This work was supported by funding from the Stanford University School of Medicine Medical Scientist Training Program (T32 GM007365) and CIRM Scholar Training 195 Program (TG2 01159) to J.O.B., a training grant from the Buck Institute for Research on Aging (T32AG00266-21) to D.I.B, and by funding from the Glenn Foundation for Medical Research, the NIH (P01 AG036695, R37 AG023806, and R01 AR062185), and the Department of Veterans Affairs (Merit Review) to T.A.R.

REFERENCES

- Pomatto LCD, and Davies KJA (2017). The role of declining adaptive homeostasis in ageing. *J. Physiol.* 595, 7275–7309. 10.1113/jp275072. [PubMed: 29028112]
- Hayflick L (2007). Biological aging is no longer an unsolved problem. *Ann. N. Y. Acad. Sci.* 1100, 1–13. 10.1196/annals.1395.001. [PubMed: 17460161]
- Gladyshev VN (2012). On the cause of aging and control of lifespan: heterogeneity leads to inevitable damage accumulation, causing aging; control of damage composition and rate of accumulation define lifespan. *Bioessays* 34, 925–929. 10.1002/bies.201200092. [PubMed: 22915358]
- Todhunter ME, Sayaman RW, Miyano M, and LaBarge MA (2018). Tissue aging: the integration of collective and variant responses of cells to entropic forces over time. *Curr. Opin. Cell Biol.* 54, 121–129. 10.1016/j.ccb.2018.05.016. [PubMed: 29908481]
- Mahmoudi S, Mancini E, Xu L, Moore A, Jahanbani F, Hebestreit K, Srinivasan R, Li X, Devarajan K, Prélot L, et al. (2019). Heterogeneity in old fibroblasts is linked to variability in reprogramming and wound healing. *Nature* 574, 553–558. 10.1038/s41586-019-1658-5. [PubMed: 31645721]
- Gladyshev VN (2014). The free radical theory of aging is dead. Long live the damage theory! *Antioxid. Redox Signal.* 20, 727–731. 10.1089/ars.2013.5228. [PubMed: 24159899]
- Barzilai N, Cuervo AM, and Austad S (2018). Aging as a Biological Target for Prevention and Therapy. *JAMA* 320, 1321–1322. 10.1001/jama.2018.9562. [PubMed: 30242337]
- Holliday R (2006). Aging is no longer an unsolved problem in biology. *Ann. N. Y. Acad. Sci.* 1067, 1–9. 10.1196/annals.1354.002.
- Miller RA (2002). Extending life: scientific prospects and political obstacles. *Milbank Q.* 80, 155–174. 10.1111/1468-0009.00006. [PubMed: 11933792]
- Holliday R (2009). The extreme arrogance of anti-aging medicine. *Biogerontology* 10, 223–228. 10.1007/s10522-008-9170-6. [PubMed: 18726707]
- Conboy IM, Conboy MJ, Smythe GM, and Rando TA (2003). Notch-mediated restoration of regenerative potential to aged muscle. *Science* 302, 1575–1577. 10.1126/science.1087573. [PubMed: 14645852]
- Brack AS, and Muñoz-Cánoves P (2016). The ins and outs of muscle stem cell aging. *Skelet. Muscle* 6, 1. 10.1186/s13395-016-0072-z. [PubMed: 26783424]
- Muñoz-Cánoves P, Neves J, and Sousa-Victor P (2020). Understanding muscle regenerative decline with aging: new approaches to bring back youthfulness to aged stem cells. *FEBS J.* 287, 406–416. 10.1111/febs.15182. [PubMed: 31854082]
- Schwörer S, Becker F, Feller C, Baig AH, Köber U, Henze H, Kraus JM, Xin B, Lechel A, Lipka DB, et al. (2016). Epigenetic stress responses induce muscle stem-cell ageing by Hoxa9 developmental signals. *Nature* 540, 428–432. 10.1038/nature20603. [PubMed: 27919074]
- Liu L, Cheung TH, Charville GW, Hurgo BMC, Leavitt T, Shih J, Brunet A, and Rando TA (2013). Chromatin modifications as determinants of muscle stem cell quiescence and chronological aging. *Cell Rep.* 4, 189–204. 10.1016/j.celrep.2013.05.043. [PubMed: 23810552]
- Hernando-Herraez I, Evano B, Stubbs T, Commere P-H, Jan Bonder M, Clark S, Andrews S, Tajbakhsh S, and Reik W (2019). Ageing affects DNA methylation drift and transcriptional

- cell-to-cell variability in mouse muscle stem cells. *Nat. Commun.* 10, 4361. 10.1038/s41467-019-12293-4. [PubMed: 31554804]
17. Solanas G, Peixoto FO, Perdiguero E, Jardí M, Ruiz-Bonilla V, Datta D, Symeonidi A, Castellanos A, Welz P-S, Caballero JM, et al. (2017). Aged Stem Cells Reprogram Their Daily Rhythmic Functions to Adapt to Stress. *Cell* 170, 678–692.e20. 10.1016/j.cell.2017.07.035. [PubMed: 28802040]
 18. Pala F, Di Girolamo D, Mella S, Yennek S, Chatre L, Ricchetti M, and Tajbakhsh S (2018). Distinct metabolic states govern skeletal muscle stem cell fates during prenatal and postnatal myogenesis. *J. Cell Sci.* 131. 10.1242/jcs.212977.
 19. Lukjanenko L, Jung MJ, Hegde N, Perruisseau-Carrier C, Migliavacca E, Rozo M, Karaz S, Jacot G, Schmidt M, Li L, et al. (2016). Loss of fibronectin from the aged stem cell niche affects the regenerative capacity of skeletal muscle in mice. *Nat. Med.* 22, 897–905. 10.1038/nm.4126. [PubMed: 27376579]
 20. Sousa-Victor P, Gutarra S, García-Prat L, Rodríguez-Ubrea J, Ortet L, Ruiz-Bonilla V, Jardí M, Ballestar E, González S, Serrano AL, et al. (2014). Geriatric muscle stem cells switch reversible quiescence into senescence. *Nature* 506, 316–321. 10.1038/nature13013. [PubMed: 24522534]
 21. Bernet JD, Doles JD, Hall JK, Kelly Tanaka K, Carter TA, and Olwin BB (2014). p38 MAPK signaling underlies a cell-autonomous loss of stem cell self-renewal in skeletal muscle of aged mice. *Nat. Med.* 20, 265–271. 10.1038/nm.3465. [PubMed: 24531379]
 22. Brett JO, Arjona M, Ikeda M, Quarta M, de Morrée A, Egner IM, Perandini LA, Ishak HD, Goshayeshi A, Benjamin DI, et al. (2020). Exercise rejuvenates quiescent skeletal muscle stem cells in old mice through restoration of Cyclin D1. *Nat. Metab.* 2, 307–317. 10.1038/s42255-020-0190-0. [PubMed: 32601609]
 23. Shcherbina A, Larouche J, Fraczek P, Yang BA, Brown LA, Markworth JF, Chung CH, Khaliq M, de Silva K, Choi JJ, et al. (2020). Dissecting Murine Muscle Stem Cell Aging through Regeneration Using Integrative Genomic Analysis. *Cell Rep.* 32, 107964. 10.1016/j.celrep.2020.107964. [PubMed: 32726628]
 24. Liu L, Charville GW, Cheung TH, Yoo B, Santos PJ, Schroeder M, and Rando TA (2018). Impaired Notch Signaling Leads to a Decrease in p53 Activity and Mitotic Catastrophe in Aged Muscle Stem Cells. *Cell Stem Cell* 23, 544–556.e4. 10.1016/j.stem.2018.08.019. [PubMed: 30244867]
 25. Tierney MT, Stec MJ, Rulands S, Simons BD, and Sacco A (2018). Muscle Stem Cells Exhibit Distinct Clonal Dynamics in Response to Tissue Repair and Homeostatic Aging. *Cell Stem Cell* 22, 119–127.e3. 10.1016/j.stem.2017.11.009. [PubMed: 29249462]
 26. Li L, Rozo M, Yue S, Zheng X, Tan F, Lepper C, and Fan C-M (2019). Muscle stem cell renewal suppressed by Gas1 can be reversed by GDNF in mice. *Nat. Metab.* 1, 985–995. 10.1038/s42255-019-0110-3. [PubMed: 32021964]
 27. Kimmel JC, Hwang AB, Scaramozza A, Marshall WF, and Brack AS (2020). Aging induces aberrant state transition kinetics in murine muscle stem cells. *Development* 147. 10.1242/dev.183855.
 28. Chakkalakal JV, Jones KM, Basson MA, and Brack AS (2012). The aged niche disrupts muscle stem cell quiescence. *Nature* 490, 355–360. 10.1038/nature11438. [PubMed: 23023126]
 29. Bou Sleiman M, Jha P, Houtkooper R, Williams RW, Wang X, and Auwerx J (2020). The Gene-Regulatory Footprint of Aging Highlights Conserved Central Regulators. *Cell Rep.* 32, 108203. 10.1016/j.celrep.2020.108203. [PubMed: 32997995]
 30. Machado L, Esteves de Lima J, Fabre O, Proux C, Legendre R, Szegedi A, Varet H, Ingerslev LR, Barrès R, Relaix F, et al. (2017). In Situ Fixation Redefines Quiescence and Early Activation of Skeletal Muscle Stem Cells. *Cell Rep.* 21, 1982–1993. 10.1016/j.celrep.2017.10.080. [PubMed: 29141227]
 31. Horvath S, and Raj K (2018). DNA methylation-based biomarkers and the epigenetic clock theory of ageing. *Nat. Rev. Genet.* 19, 371–384. 10.1038/s41576-018-0004-3. [PubMed: 29643443]
 32. Wu H, Wang C, and Wu Z (2013). A new shrinkage estimator for dispersion improves differential expression detection in RNA-seq data. *Biostatistics* 14, 232–243. 10.1093/biostatistics/kxs033. [PubMed: 23001152]

33. Ziller MJ, Gu H, Müller F, Donaghey J, Tsai LT-Y, Kohlbacher O, De Jager PL, Rosen ED, Bennett DA, Bernstein BE, et al. (2013). Charting a dynamic DNA methylation landscape of the human genome. *Nature* 500, 477–481. 10.1038/nature12433. [PubMed: 23925113]
34. Sun D, Luo M, Jeong M, Rodriguez B, Xia Z, Hannah R, Wang H, Le T, Faull KF, Chen R, et al. (2014). Epigenomic profiling of young and aged HSCs reveals concerted changes during aging that reinforce self-renewal. *Cell Stem Cell* 14, 673–688. 10.1016/j.stem.2014.03.002. [PubMed: 24792119]
35. Weber M, Hellmann I, Stadler MB, Ramos L, Pääbo S, Rebhan M, and Schübeler D (2007). Distribution, silencing potential and evolutionary impact of promoter DNA methylation in the human genome. *Nat. Genet.* 39, 457–466. 10.1038/ng1990. [PubMed: 17334365]
36. Brinkman AB, Gu H, Bartels SJJ, Zhang Y, Matarese F, Simmer F, Marks H, Bock C, Gnirke A, Meissner A, et al. (2012). Sequential ChIP-bisulfite sequencing enables direct genome-scale investigation of chromatin and DNA methylation cross-talk. *Genome Res.* 22, 1128–1138. 10.1101/gr.133728.111. [PubMed: 22466170]
37. Manzo M, Wirz J, Ambrosi C, Villaseñor R, Roschitzki B, and Baubec T (2017). Isoform-specific localization of DNMT3A regulates DNA methylation fidelity at bivalent CpG islands. *EMBO J.* 36, 3421–3434. 10.15252/embj.201797038. [PubMed: 29074627]
38. Viré E, Brenner C, Deplus R, Blanchon L, Fraga M, Didelot C, Morey L, Van Eynde A, Bernard D, Vanderwinden J-M, et al. (2006). The Polycomb group protein EZH2 directly controls DNA methylation. *Nature* 439, 871–874. 10.1038/nature04431. [PubMed: 16357870]
39. Statham AL, Robinson MD, Song JZ, Coolen MW, Stirzaker C, and Clark SJ (2012). Bisulfite sequencing of chromatin immunoprecipitated DNA (BisChIP-seq) directly informs methylation status of histone-modified DNA. *Genome Res.* 22, 1120–1127. 10.1101/gr.132076.111. [PubMed: 22466171]
40. Tanay A, O'Donnell AH, Damelin M, and Bestor TH (2007). Hyperconserved CpG domains underlie Polycomb-binding sites. *Proc. Natl. Acad. Sci. U. S. A.* 104, 5521–5526. 10.1073/pnas.0609746104. [PubMed: 17376869]
41. Lindroth AM, Park YJ, McLean CM, Dokshin GA, Persson JM, Herman H, Pasini D, Miró X, Donohoe ME, Lee JT, et al. (2008). Antagonism between DNA and H3K27 methylation at the imprinted Rasgrf1 locus. *PLoS Genet.* 4, e1000145. 10.1371/journal.pgen.1000145. [PubMed: 18670629]
42. Boulard M, Edwards JR, and Bestor TH (2015). FBXL10 protects Polycomb-bound genes from hypermethylation. *Nat. Genet.* 47, 479–485. 10.1038/ng.3272. [PubMed: 25848754]
43. Zhao X, Wang X, Li Q, Chen W, Zhang N, Kong Y, Lv J, Cao L, Lin D, Wang X, et al. (2018). FBXL10 contributes to the development of diffuse large B-cell lymphoma by epigenetically enhancing ERK1/2 signaling pathway. *Cell Death Dis.* 9, 46. 10.1038/s41419-017-0066-8. [PubMed: 29352142]
44. Eichenfield DZ, Troutman TD, Link VM, Lam MT, Cho H, Gosselin D, Spann NJ, Lesch HP, Tao J, Muto J, et al. (2016). Tissue damage drives co-localization of NF- κ B, Smad3, and Nrf2 to direct Rev-erb sensitive wound repair in mouse macrophages. *Elife* 5. 10.7554/eLife.13024.
45. Benayoun BA, Pollina EA, Ucar D, Mahmoudi S, Karra K, Wong ED, Devarajan K, Daugherty AC, Kundaje AB, Mancini E, et al. (2014). H3K4me3 breadth is linked to cell identity and transcriptional consistency. *Cell* 158, 673–688. 10.1016/j.cell.2014.06.027. [PubMed: 25083876]
46. Kanehisa M, and Goto S (2000). KEGG: kyoto encyclopedia of genes and genomes. *Nucleic Acids Res.* 28, 27–30. 10.1093/nar/28.1.27. [PubMed: 10592173]
47. Pinu FR, Beale DJ, Paten AM, Kouremenos K, Swarup S, Schirra HJ, and Wishart D (2019). Systems Biology and Multi-Omics Integration: Viewpoints from the Metabolomics Research Community. *Metabolites* 9. 10.3390/metabo9040076.
48. Pihur V, Datta S, and Datta S (2009). RankAggreg, an R package for weighted rank aggregation. *BMC Bioinformatics* 10, 62. 10.1186/1471-2105-10-62. [PubMed: 19228411]
49. Kolde R, Laur S, Adler P, and Vilo J (2012). Robust rank aggregation for gene list integration and meta-analysis. *Bioinformatics* 28, 573–580. 10.1093/bioinformatics/btr709. [PubMed: 22247279]

50. Mandavilli BS, and Janes MS (2010). Detection of intracellular glutathione using ThiolTracker violet stain and fluorescence microscopy. *Curr. Protoc. Cytom.* Chapter 9, Unit 9.35. 10.1002/0471142956.cy0935s53.
51. Killackey SA, Philpott DJ, and Girardin SE (2020). Mitophagy pathways in health and disease. *J. Cell Biol.* 219. 10.1083/jcb.202004029.
52. Forman HJ, Zhang H, and Rinna A (2009). Glutathione: overview of its protective roles, measurement, and biosynthesis. *Mol. Aspects Med.* 30, 1–12. 10.1016/j.mam.2008.08.006. [PubMed: 18796312]
53. Köhler E, Barrach H-J, and Neubert D (1970). Inhibition of NADP dependent oxidoreductases by the 6-aminonicotinamide analogue of NADP. *FEBS Lett.* 6, 225–228. 10.1016/0014-5793(70)80063-1. [PubMed: 11947380]
54. Griffith OW, and Meister A (1979). Potent and specific inhibition of glutathione synthesis by buthionine sulfoximine (S-n-butyl homocysteine sulfoximine). *J. Biol. Chem.* 254, 7558–7560. [PubMed: 38242]
55. Xie X, Lu J, Kulbokas EJ, Golub TR, Mootha V, Lindblad-Toh K, Lander ES, and Kellis M (2005). Systematic discovery of regulatory motifs in human promoters and 3' UTRs by comparison of several mammals. *Nature* 434, 338–345. 10.1038/nature03441. [PubMed: 15735639]
56. Adler AS, Sinha S, Kawahara TLA, Zhang JY, Segal E, and Chang HY (2007). Motif module map reveals enforcement of aging by continual NF-kappaB activity. *Genes Dev.* 21, 3244–3257. 10.1101/gad.1588507. [PubMed: 18055696]
57. Tilstra JS, Robinson AR, Wang J, Gregg SQ, Clauson CL, Reay DP, Nasto LA, St Croix CM, Usas A, Vo N, et al. (2012). NF-κB inhibition delays DNA damage-induced senescence and aging in mice. *J. Clin. Invest.* 122, 2601–2612. 10.1172/JCI45785. [PubMed: 22706308]
58. Carlson ME, Hsu M, and Conboy IM (2008). Imbalance between pSmad3 and Notch induces CDK inhibitors in old muscle stem cells. *Nature* 454, 528–532. 10.1038/nature07034. [PubMed: 18552838]
59. Wardyn JD, Ponsford AH, and Sanderson CM (2015). Dissecting molecular cross-talk between Nrf2 and NF-κB response pathways. *Biochem. Soc. Trans.* 43, 621–626. 10.1042/BST20150014. [PubMed: 26551702]
60. Oh J, Sinha I, Tan KY, Rosner B, Dreyfuss JM, Gjata O, Tran P, Shoelson SE, and Wagers AJ (2016). Age-associated NF-κB signaling in myofibers alters the satellite cell niche and re-strains muscle stem cell function. *Aging (Albany, NY)*. 8, 2871–2896. 10.18632/aging.101098. [PubMed: 27852976]
61. Straughn AR, Hindi SM, Xiong G, and Kumar A (2019). Canonical NF-κB signaling regulates satellite stem cell homeostasis and function during regenerative myogenesis. *J. Mol. Cell Biol.* 11, 53–66. 10.1093/jmcb/mjy053. [PubMed: 30239789]
62. Shin H-M, Kim M-H, Kim BH, Jung S-H, Kim YS, Park HJ, Hong JT, Min KR, and Kim Y (2004). Inhibitory action of novel aromatic diamine compound on lipopolysaccharide-induced nuclear translocation of NF-kappaB without affecting IkappaB degradation. *FEBS Lett.* 571, 50–54. 10.1016/j.febslet.2004.06.056. [PubMed: 15280016]
63. Conboy IM, Conboy MJ, Wagers AJ, Girma ER, Weissman IL, and Rando TA (2005). Rejuvenation of aged progenitor cells by exposure to a young systemic environment. *Nature* 433, 760–764. 10.1038/nature03260. [PubMed: 15716955]
64. Conboy IM, and Rando TA (2012). Heterochronic parabiosis for the study of the effects of aging on stem cells and their niches. *Cell Cycle* 11, 2260–2267. 10.4161/cc.20437. [PubMed: 22617385]
65. Brandman O, and Meyer T (2008). Feedback loops shape cellular signals in space and time. *Science* 322, 390–395. 10.1126/science.1160617. [PubMed: 18927383]
66. Chung M, Liu C, Yang HW, Köberlin MS, Cappell SD, and Meyer T (2019). Transient Hysteresis in CDK4/6 Activity Underlies Passage of the Restriction Point in G1. *Mol. Cell* 76, 562–573.e4. 10.1016/j.molcel.2019.08.020. [PubMed: 31543423]
67. Prestigiacomo V, and Suter-Dick L (2018). Nrf2 protects stellate cells from Smad-dependent cell activation. *PLoS One* 13, e0201044. 10.1371/journal.pone.0201044. [PubMed: 30028880]

68. Gañán-Gómez I, Wei Y, Yang H, Boyano-Adánez MC, and García-Manero G (2013). Oncogenic functions of the transcription factor Nrf2. *Free Radic. Biol. Med.* 65, 750–764. 10.1016/j.freeradbiomed.2013.06.041. [PubMed: 23820265]
69. Christov C, Chrétien F, Abou-Khalil R, Bassez G, Vallet G, Authier F-J, Bassaglia Y, Shinin V, Tajbakhsh S, Chazaud B, et al. (2007). Muscle satellite cells and endothelial cells: close neighbors and privileged partners. *Mol. Biol. Cell* 18, 1397–1409. 10.1091/mbc.e06-08-0693. [PubMed: 17287398]
70. Verma M, Asakura Y, Murakonda BSR, Pengo T, Latroche C, Chazaud B, McLoon LK, and Asakura A (2018). Muscle Satellite Cell Cross-Talk with a Vascular Niche Maintains Quiescence via VEGF and Notch Signaling. *Cell Stem Cell* 23, 530–543.e9. 10.1016/j.stem.2018.09.007. [PubMed: 30290177]
71. Du H, Shih C-H, Wosczyzna MN, Mueller AA, Cho J, Aggarwal A, Rando TA, and Feldman BJ (2017). Macrophage-released ADAMTS1 promotes muscle stem cell activation. *Nat. Commun.* 8, 669. 10.1038/s41467-017-00522-7. [PubMed: 28939843]
72. Murphy MM, Lawson JA, Mathew SJ, Hutcheson DA, and Kardon G (2011). Satellite cells, connective tissue fibroblasts and their interactions are crucial for muscle regeneration. *Development* 138, 3625–3637. 10.1242/dev.064162. [PubMed: 21828091]
73. Wosczyzna MN, Konishi CT, Perez Carbajal EE, Wang TT, Walsh RA, Gan Q, Wagner MW, and Rando TA (2019). Mesenchymal Stromal Cells Are Required for Regeneration and Homeostatic Maintenance of Skeletal Muscle. *Cell Rep.* 27, 2029–2035.e5. 10.1016/j.celrep.2019.04.074. [PubMed: 31091443]
74. Dumont NA, Wang YX, von Maltzahn J, Pasut A, Bentzinger CF, Brun CE, and Rudnicki MA (2015). Dystrophin expression in muscle stem cells regulates their polarity and asymmetric division. *Nat. Med.* 21, 1455–1463. 10.1038/nm.3990. [PubMed: 26569381]
75. Richie JP (1992). The role of glutathione in aging and cancer. *Exp. Gerontol.* 27, 615–626. 10.1016/0531-5565(92)90015-r. [PubMed: 1426093]
76. Haug K, Cochrane K, Nainala VC, Williams M, Chang J, Jayaseelan KV, and O'Donovan C (2020). MetaboLights: a resource evolving in response to the needs of its scientific community. *Nucleic Acids Res.* 48, D440–D444. 10.1093/nar/gkz1019. [PubMed: 31691833]
77. Edgar R, Domrachev M, and Lash AE (2002). Gene Expression Omnibus: NCBI gene expression and hybridization array data repository. *Nucleic Acids Res.* 30, 207–210. 10.1093/nar/30.1.207. [PubMed: 11752295]
78. Dobin A, Davis CA, Schlesinger F, Drenkow J, Zaleski C, Jha S, Batut P, Chaisson M, and Gingeras TR (2013). STAR: ultrafast universal RNA-seq aligner. *Bioinformatics* 29, 15–21. 10.1093/bioinformatics/bts635. [PubMed: 23104886]
79. Liao Y, Smyth GK, and Shi W (2014). featureCounts: an efficient general purpose program for assigning sequence reads to genomic features. *Bioinformatics* 30, 923–930. 10.1093/bioinformatics/btt656. [PubMed: 24227677]
80. Robinson MD, McCarthy DJ, and Smyth GK (2010). edgeR: a Bioconductor package for differential expression analysis of digital gene expression data. *Bioinformatics* 26, 139–140. 10.1093/bioinformatics/btp616. [PubMed: 19910308]
81. Xu T, Park SK, Venable JD, Wohlschlegel JA, Diedrich JK, Cociorva D, Lu B, Liao L, Hewel J, Han X, et al. (2015). ProLuCID: An improved SEQUEST-like algorithm with enhanced sensitivity and specificity. *J. Proteomics* 129, 16–24. 10.1016/j.jprot.2015.07.001. [PubMed: 26171723]
82. Li X, and Snyder MP (2016). Yeast longevity promoted by reversing aging-associated decline in heavy isotope content. *NPJ aging Mech. Dis.* 2, 16004. 10.1038/npjamd.2016.4.
83. Guan S, Price JC, Prusiner SB, Ghaemmaghami S, and Burlingame AL (2011). A data processing pipeline for mammalian proteome dynamics studies using stable isotope metabolic labeling. *Mol. Cell. Proteomics* 10, M111.010728. 10.1074/mcp.M111.010728.
84. Smith CA, Want EJ, O'Maille G, Abagyan R, and Siuzdak G (2006). XCMS: processing mass spectrometry data for metabolite profiling using nonlinear peak alignment, matching, and identification. *Anal. Chem.* 78, 779–787. 10.1021/ac051437y. [PubMed: 16448051]

85. Voss B, Hanselmann M, Renard BY, Lindner MS, Köthe U, Kirchner M, and Hamprecht FA (2011). SIMA: simultaneous multiple alignment of LC/MS peak lists. *Bioinformatics* 27, 987–993. 10.1093/bioinformatics/btr051. [PubMed: 21296750]
86. Johnson WE, Li C, and Rabinovic A (2007). Adjusting batch effects in microarray expression data using empirical Bayes methods. *Biostatistics* 8, 118–127. 10.1093/biostatistics/kxj037. [PubMed: 16632515]
87. Wishart DS, Knox C, Guo AC, Eisner R, Young N, Gautam B, Hau DD, Psychogios N, Dong E, Bouatra S, et al. (2009). HMDB: a knowledgebase for the human metabolome. *Nucleic Acids Res.* 37, D603–10. 10.1093/nar/gkn810. [PubMed: 18953024]
88. Ogata H, Goto S, Sato K, Fujibuchi W, Bono H, and Kanehisa M (1999). KEGG: Kyoto Encyclopedia of Genes and Genomes. *Nucleic Acids Res.* 27, 29–34. 10.1093/nar/27.1.29. [PubMed: 9847135]
89. Breitling R, Armengaud P, Amtmann A, and Herzyk P (2004). Rank products: a simple, yet powerful, new method to detect differentially regulated genes in replicated microarray experiments. *FEBS Lett.* 573, 83–92. 10.1016/j.febslet.2004.07.055. [PubMed: 15327980]
90. Krueger F, and Andrews SR (2011). Bismark: a flexible aligner and methylation caller for Bisulfite-Seq applications. *Bioinformatics* 27, 1571–1572. 10.1093/bioinformatics/btr167. [PubMed: 21493656]
91. Karolchik D, Hinrichs AS, Furey TS, Roskin KM, Sugnet CW, Haussler D, and Kent WJ (2004). The UCSC Table Browser data retrieval tool. *Nucleic Acids Res.* 32, D493–6. 10.1093/nar/gkh103. [PubMed: 14681465]
92. Haeussler M, Zweig AS, Tyner C, Speir ML, Rosenbloom KR, Raney BJ, Lee CM, Lee BT, Hinrichs AS, Gonzalez JN, et al. (2019). The UCSC Genome Browser database: 2019 update. *Nucleic Acids Res.* 47, D853–D858. 10.1093/nar/gky1095. [PubMed: 30407534]
93. Irizarry RA, Ladd-Acosta C, Wen B, Wu Z, Montano C, Onyango P, Cui H, Gabo K, Rongione M, Webster M, et al. (2009). The human colon cancer methylome shows similar hypo- and hypermethylation at conserved tissue-specific CpG island shores. *Nat. Genet.* 41, 178–186. 10.1038/ng.298. [PubMed: 19151715]
94. Kishore K, de Pretis S, Lister R, Morelli MJ, Bianchi V, Amati B, Ecker JR, and Pelizzola M (2015). methylPipe and compEpiTools: a suite of R packages for the integrative analysis of epigenomics data. *BMC Bioinformatics* 16, 313. 10.1186/s12859-015-0742-6. [PubMed: 26415965]
95. Ball MP, Li JB, Gao Y, Lee J-H, LeProust EM, Park I-H, Xie B, Daley GQ, and Church GM (2009). Targeted and genome-scale strategies reveal gene-body methylation signatures in human cells. *Nat. Biotechnol.* 27, 361–368. 10.1038/nbt.1533. [PubMed: 19329998]
96. Subramanian A, Tamayo P, Mootha VK, Mukherjee S, Ebert BL, Gillette MA, Paulovich A, Pomeroy SL, Golub TR, Lander ES, et al. (2005). Gene set enrichment analysis: a knowledge-based approach for interpreting genome-wide expression profiles. *Proc. Natl. Acad. Sci. U. S. A.* 102, 15545–15550. 10.1073/pnas.0506580102. [PubMed: 16199517]
97. Hernández-de-Diego R, Tarazona S, Martínez-Mira C, Balzano-Nogueira L, FurióTari P, Pappas GJJ, and Conesa A (2018). PaintOmics 3: a web resource for the pathway analysis and visualization of multi-omics data. *Nucleic Acids Res.* 46, W503–W509. 10.1093/nar/gky466. [PubMed: 29800320]
98. García-Alcalde F, García-López F, Dopazo J, and Conesa A (2011). Paintomics: a web based tool for the joint visualization of transcriptomics and metabolomics data. *Bioinformatics* 27, 137–139. 10.1093/bioinformatics/btq594. [PubMed: 21098431]
99. Varum S, Rodrigues AS, Moura MB, Momcilovic O, Easley CA 4th, Ramalho-Santos J, Van Houten B, and Schatten G (2011). Energy metabolism in human pluripotent stem cells and their differentiated counterparts. *PLoS One* 6, e20914. 10.1371/journal.pone.0020914. [PubMed: 21698063]
100. Pfaffl MW (2001). A new mathematical model for relative quantification in real-time RT-PCR. *Nucleic Acids Res.* 29, e45. 10.1093/nar/29.9.e45. [PubMed: 11328886]

101. de Morree A, Klein JDD, Gan Q, Farup J, Urtasun A, Kanugovi A, Bilen B, van Velthoven CTJ, Quarta M, and Rando TA (2019). Alternative polyadenylation of Pax3 controls muscle stem cell fate and muscle function. *Science* 366, 734–738. [10.1126/science.aax1694](https://doi.org/10.1126/science.aax1694). [PubMed: 31699935]

Author Manuscript

Author Manuscript

Author Manuscript

Author Manuscript

Highlights

- A multiomic analysis reveals that GSH metabolism is altered with age
- Old MuSCs exhibit a population dichotomy consisting of GSH^{high} and GSH^{low} cells
- Altering GSH content shifts the functional dichotomy and affects muscle regeneration
- The GSH population dichotomy is driven by NF- κ B mediated inhibition of NRF2.

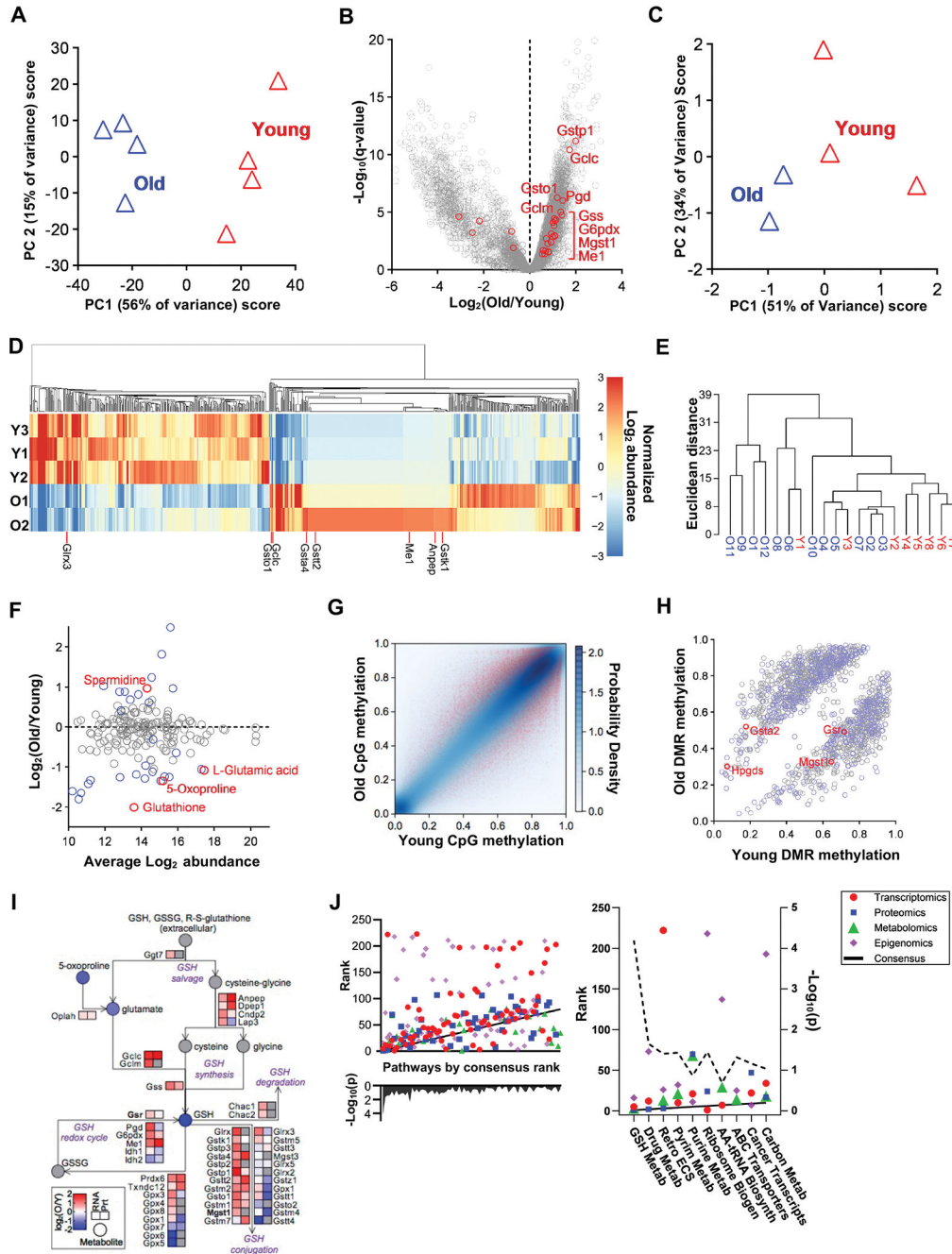


Figure 1. Multiomics identifies glutathione metabolism as altered with age in quiescent MuSCs. **A)** PCA of RNA-seq of quiescent MuSCs from young (n=4) and old (n=4) mice. Each replicate, shown as a single triangle, represents MuSCs from one mouse. **B)** Volcano plot of genes profiled by RNA-seq. Genes involved in glutathione metabolism and significantly different at FDR 5% are indicated in red. **C)** PCA of shotgun proteomics of quiescent MuSCs of young (n=3) and old (n=2) biological replicates. Each replicate, shown as a single triangle, represents MuSCs pooled from 16–20 mice. **D)** Heatmap of proteins profiled by shotgun proteomics. To facilitate visualization of genes of interest, shown are the proteins for which replicates showed reproducible behavior. Proteins involved in glutathione

metabolism are labelled. **E)** Hierarchical clustering of metabolomics of quiescent MuSCs of young (n=8) and old (n=12) biological replicates. Each replicate, shown as a single leaf, represents MuSCs pooled from 2–6 mice. **F)** M-A plot of metabolites profiled. Metabolites that are significantly different at FDR 30% are colored blue; metabolites involved in glutathione metabolism that are significantly different at this cutoff are highlighted in red. **G)** Kernel density plot of methylation levels of ~33 million individual CpGs profiled in young and old MuSCs (n=4 individual mice in each age group). CpGs significantly different at FDR 5% (~80 thousand) are plotted in red. **H)** Each DMR is shown as a point displaying young and old mean methylation levels. DMRs associated with genes are blue; DMRs associated with glutathione metabolism genes are red. **I)** Simplified diagram of mammalian glutathione metabolism depicting changes that occur with age. Boxes are genes products; circles are metabolites. Each element is colored by the old vs. young change that occurs with age; RNA changes are on the left, and protein changes are on the right. Genes with DNA methylation changes are bolded. Gray indicates no data. Only genes that are expressed in the RNA or protein datasets are shown. **J)** Consensus ranking of KEGG Pathways generated by combining the ranked pathway lists of individual datasets through rank aggregation. Pathways, ordered by consensus rank, have individual ranks across datasets shown in different colors. The p-value represents the significance of the rank vector (not the consensus rank). The left shows all the pathways for which consensus ranks were generated; the right shows the top ten.

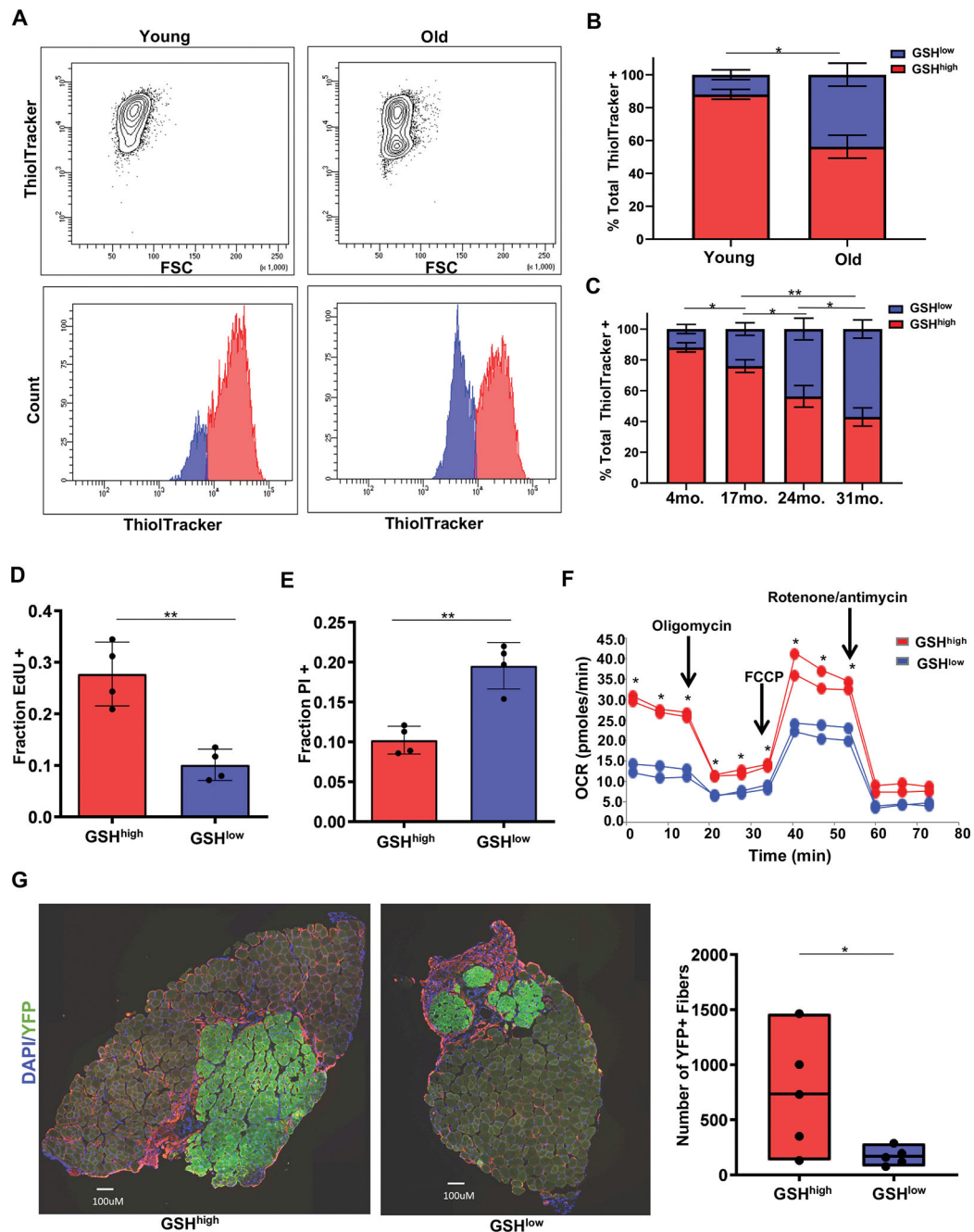


Figure 2. The bulk population of old MuSCs is comprised of GSH^{high} and GSH^{low} populations with differential functionalities.

A) Representative flow cytometry contour plots (top) and histograms (bottom) from freshly isolated MuSCs from young (4-month) and old (24-month) mice incubated for 30 minutes with ThiolTracker Violet. The GSH^{high} population is shaded red, and the GSH^{low} population is shaded blue. **B)** Percentage of GSH^{high} and GSH^{low} cells in freshly isolated MuSCs from young and old mice (n=5–6). **C)** Percentage of GSH^{high} and GSH^{low} cells in freshly isolated MuSCs from mice over an age gradient (n=4–6). **D)** EdU incorporation in GSH^{high} and GSH^{low} MuSCs isolated from 24-month-old mice and maintained in culture for 48

hours in the continuous presence of EdU (n=4). **E**) Cell death (PI staining) in GSH^{high} and GSH^{low} MuSCs isolated from 24-month-old mice and maintained in culture for 48 hours (n=4). **F**) Seahorse assay comparing 2×10^5 GSH^{high} and GSH^{low} MuSCs isolated from 24-month-old mice. Each replicate represents a pool of 4–5 mice (n=2 replicates). **G**) Representative images (left) of YFP-expressing GSH^{high} and GSH^{low} MuSCs that were transplanted into pre-injured and pre-irradiated TA muscles. Cryosections, harvested 28 days after transplantation, were analyzed for YFP expression, and the number of YFP-positive fibers was quantified (right). (n=5). Error bars represent SEM. *p < 0.05; **p < 0.01.

Author Manuscript

Author Manuscript

Author Manuscript

Author Manuscript

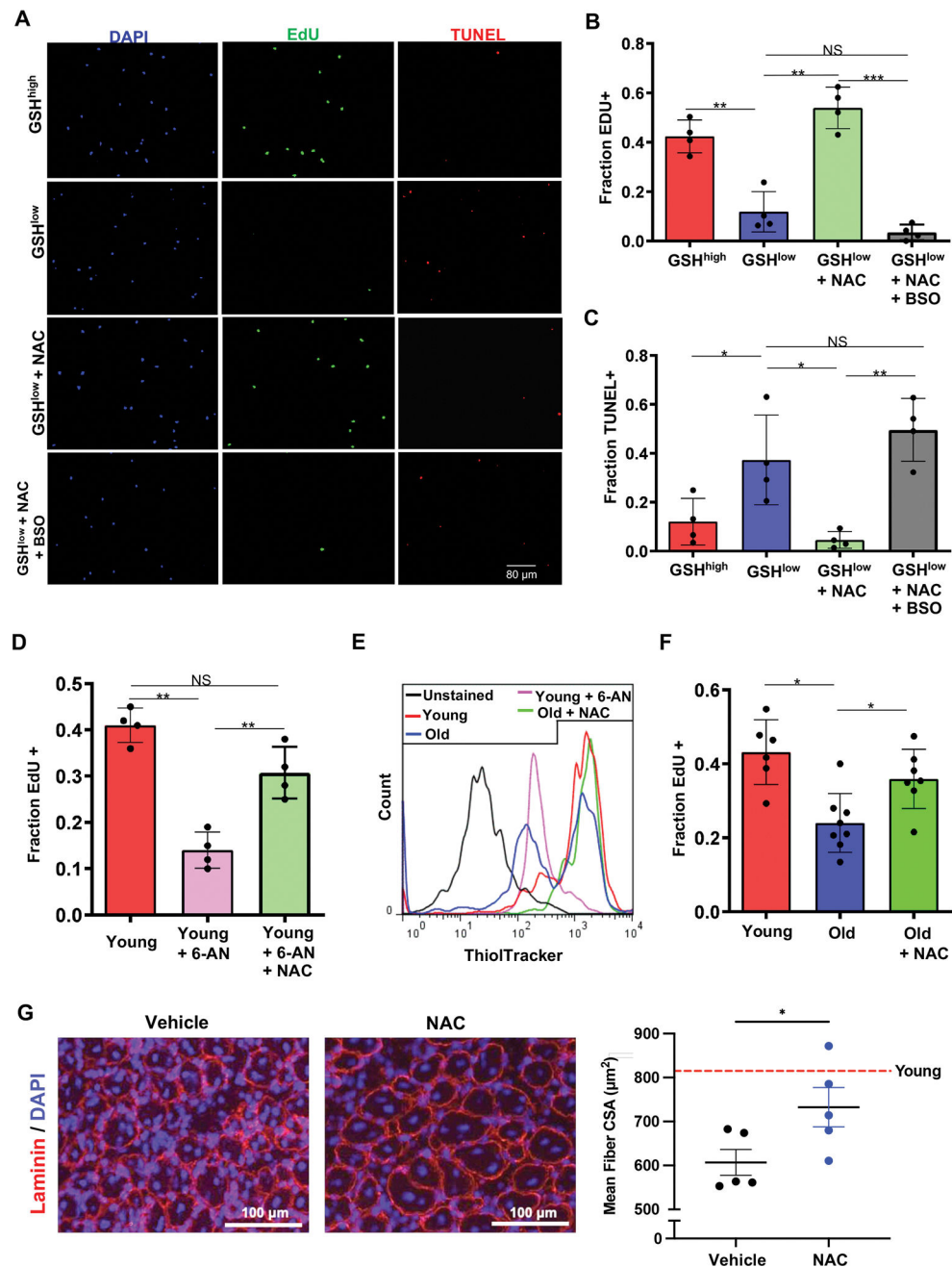


Figure 3. GSH levels causally determine MuSC function.

A) Representative images from freshly isolated GSH^{high} MuSCs, GSH^{low} MuSCs, and GSH^{low} MuSCs treated for 48 hours with either 2 mM NAC or the combination of 2 mM NAC with 1 mM BSO (an inhibitor of GCS). All cells were grown in culture for 48 hours in the continuous presence of EdU. **B-C)** Quantification of EdU-positive (b) and TUNEL-positive (c) cells from the experiment as described in (a) (n=4). **D)** EdU incorporation in MuSCs isolated from young (4-month-old) mice treated with either vehicle, 10 μM 6-AN, or the combination of 10 μM 6-AN plus 2 mM NAC for 48 hours. All cells were grown in culture for 48 hours in the continuous presence of EdU. **E)** Representative flow cytometry

plot displaying ThiolTracker intensity in young MuSCs treated with either vehicle or 10 μ M 6-AN for 48 hours as well as old MuSCs treated with either vehicle or with 2 mM NAC for 48 hours. **F)** In vivo MuSC EdU incorporation in mice injured with BaCl₂ and subsequently injected intramuscularly with either 150 mg/kg NAC or vehicle. 2 days after injury, mice were injected with 50 mg/kg EdU i.p., and MuSCs were isolated 12 hours after EdU administration (n=6–8). Error bars represent SEM. *p < 0.05; **p < 0.01; ***p < 0.001; NS, not significant.

Author Manuscript

Author Manuscript

Author Manuscript

Author Manuscript

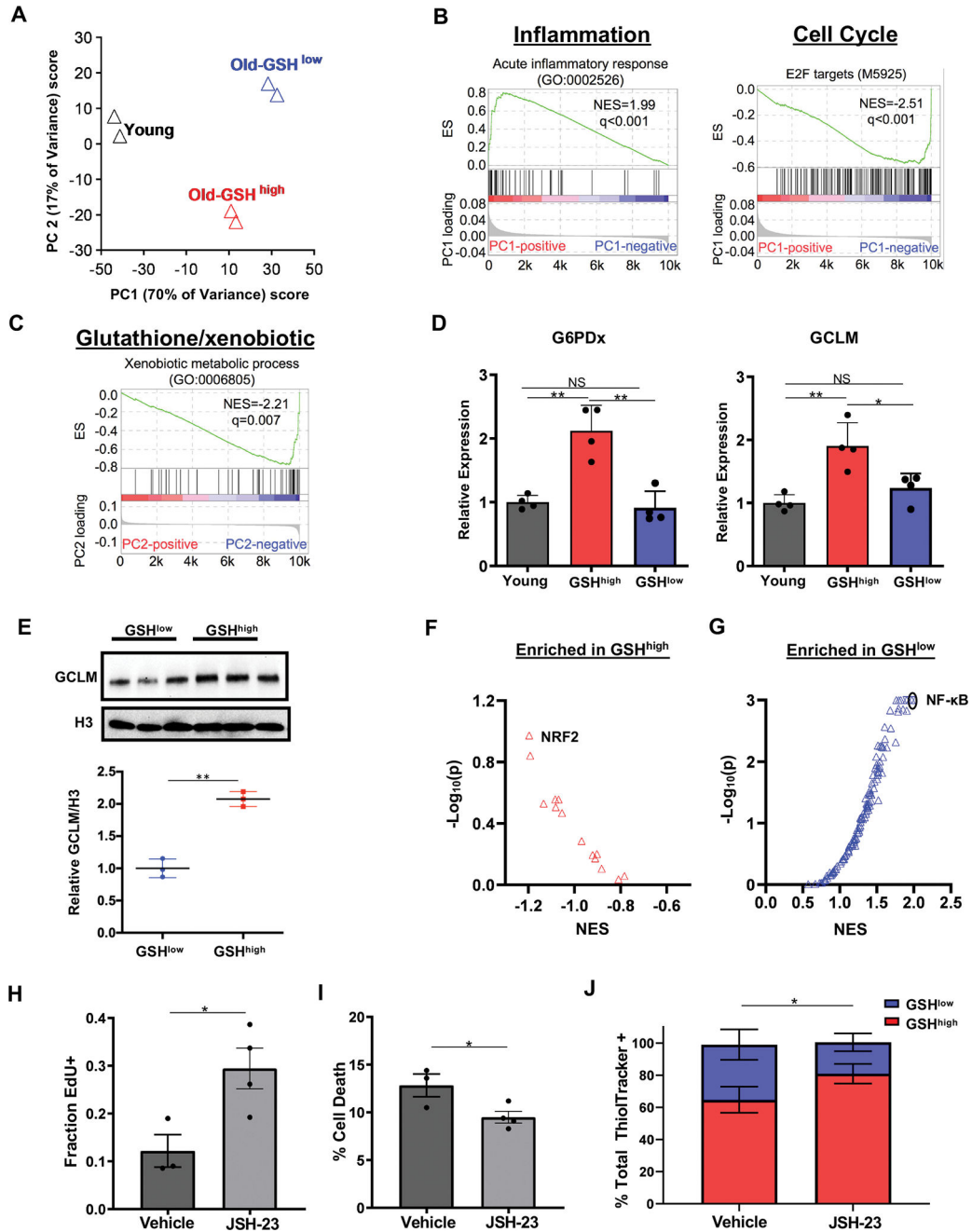
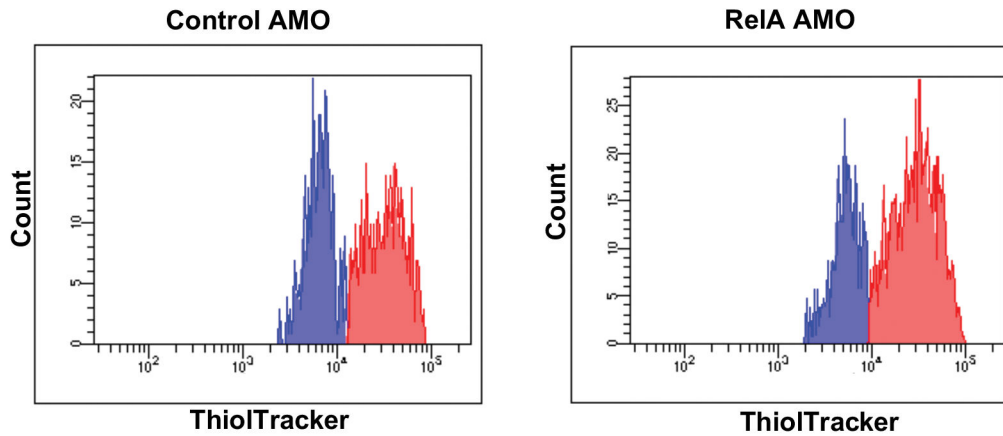


Figure 4. Transcriptomic profiling of GSH^{high} and GSH^{low} MuSCs reveals an NF-κB-mediated failure of GSH^{low} cells to engage compensatory GSH biosynthetic pathways.

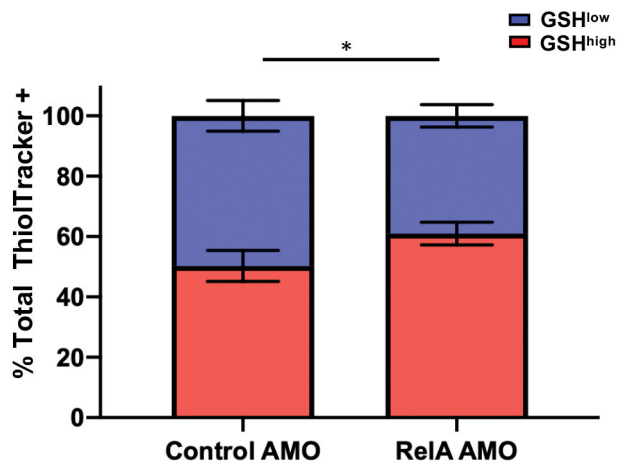
A) PCA of RNA-seq profiles of freshly isolated GSH^{high}, GSH^{low}, and total young MuSCs. Each biological replicate (triangle) represents MuSCs pooled from 3–4 mice (n=2 biological replicates). **B)** GSEA signature plots for inflammation and cell-cycle gene sets with genes ranked by PC1 (“biological age axis”) loading. ES: enrichment score, NES: normalized enrichment score. **C)** GSEA signature plot for a gene set representing GSH metabolism and the general xenobiotic response with genes ranked by PC2 (“glutathione turnover axis”) loading. **D)** RT-qPCR for G6PDx (left) and GCLM (right) in GSH^{high}, GSH^{low},

and total young MuSCs. MuSCs were derived from mice independent from those used for the RNA-seq experiment. Ct values were normalized first to GAPDH and then to the mean of the young levels (n=4). **E)** Western blot analysis (top) and quantification (bottom) of GCLM protein in GSH^{high} and GSH^{low} MuSCs isolated from 27-month-old mice. Total Histone H3 was used as a loading control. Each replicate represents a pool of 3–4 mice (n=3 replicates) **F-G)** GSEA results using predicted conserved transcription factor target (TFT) gene sets in the MSigDB. Predicted Nrf2 targets are enriched among GSH^{high}-upregulated genes, and predicted NF- κ B targets are enriched among GSH^{low}-upregulated genes. **H)** EdU incorporation in MuSCs isolated from mice treated for 5 days with either 2 mg/kg/day of the NF- κ B inhibitor JSH-23 or vehicle. MuSCs were maintained in culture for 48 hours in the continuous presence of EdU (n=4). **I)** Cell death as the percentage of cells that are PI-positive from the MuSCs described in (g) following 48 hours in culture. **J)** Percentage of GSH^{high} and GSH^{low} MuSCs using the ThiolTracker probe from the experiment described in (g). Error bars represent SEM. *p < 0.05; **p < 0.01; NS, not significant.

A



B



C

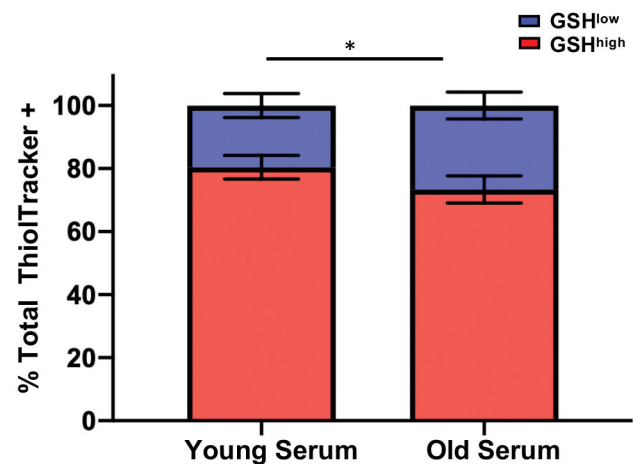


Figure 5. NF- κ B AMO treatment and old serum transfer can alter the proportion of GSH^{high} and GSH^{low} MuSCs

A) Representative FACS plots measuring ThiolTracker content of MuSCs isolated from 27-month-old mice treated with control AMO (top) or RelA AMO (bottom). B) Percentage of GSH^{high} and GSH^{low} MuSCs isolated from 27-month-old mice treated with control AMO or RelA AMO (n=4). C) Percentage of GSH^{high} and GSH^{low} MuSCs isolated from young mice injected with young serum or old serum (n=4). Error bars represent SEM. *p < 0.05

KEY RESOURCES TABLE

REAGENT or RESOURCE	SOURCE	IDENTIFIER
Antibodies		
Anti-mouse CD31-FITC, Clone MEC13.3	BioLegend	102506; RRID:AB_312913
Anti-mouse CD31-APC, Clone MEC13.3	BioLegend	102510; RRID:AB_312917
Anti-mouse CD45-FITC, Clone 30-F11	BioLegend	103108; RRID:AB_312973
Anti-mouse CD45-APC, Clone 30-F11	BioLegend	103112; RRID:AB_312977
Anti-mouse Ly-6A/E(Sca1)-Pacific Blue, Clone D7	BioLegend	108120; RRID:AB_493273
Anti-mouse CD106 (VCAM1)-PE/Cy7, Clone 429(MVCAM.A)	BioLegend	105720; RRID:AB_2214046
Anti-laminin 2a	Abcam	11576; RRID:AB_298180
Bacterial and Virus Strains		
Biological Samples		
Chemicals, Peptides, and Recombinant Proteins		
N-acetyl-L-cysteine (NAC)	Sigma-Aldrich	A7250
6-aminonicotinamide (6-AN)	Cayman Chemical	10009315
JSH-23	Selleck Chemicals	S7351
L-buthionine sulfoximine (BSO)	Sigma-Aldrich	B2515
5-ethynyl-2'-deoxyuridine (EdU)	Invitrogen (ex vivo); Abcam (in vivo)	C10339 (Invitrogen); ab146186 (Abcam)
40,6-diamidino-2-phenylindole (DAPI)	Thermo Fisher	D1306
Propidium iodide	Thermo Fisher	P3566
ThiolTracker Violet	Thermo Fisher	T10095
MitoTracker Green FM	Thermo Fisher	
MitoSOX Red	Thermo Fisher	M36008
Tamoxifen	Sigma	T5648
DMSO	Sigma	41639
Chloroquine diphosphate salt	Sigma	C6628
Critical Commercial Assays		
In Situ Cell Death Detection Kit, TMR red (TUNEL)	Sigma-Aldrich	12156792910
FITC Annexin V Apoptosis Detection Kit with 7-AAD	BioLegend	640922

REAGENT or RESOURCE	SOURCE	IDENTIFIER
Click-iT Edu Imaging Kit	Thermo Fisher	C10340
Deposited Data		
Metabolomics data have been deposited to the EMBL-EBI MetaboLights database(Haug et al., 2020) with the identifier MTBLS1779. Sequencing data have been deposited in NCBI's Gene Expression Omnibus (GEO)(Edgar et al., 2002) with accession number GSE152798.		
Raw data used to generate graphs and western blots used to are included in supplemental file Data S1		
Experimental Models: Cell Lines		
Experimental Models: Organisms/Strains		
Mouse: C57BL/6J JAX or NIA	JAX or NIA	Catalog # 000664 RRID:IMSR_JAX:000664
Mouse: B6.129X1- <i>Gt(ROSA)26Sor^{tm1(EYFP)Cos/J}</i>	JAX	Catalog # 006148 RRID:IMSR_JAX:006148
Mouse: <i>Pax7^{tm1(cre/Esr1*)Cklr}</i> (or <i>Pax7^{CreER/CreER}</i>)	(Nishijo et al., 2009)	RRID:IMSR_NCIMR:01XBS
Mouse: NOD.Cg- <i>Prkdc^{scid}Il2rg^{tm1Wjl/SzJ}</i>	JAX	Catalog # 005557 RRID:IMSR_JAX:005557
Oligonucleotides		
G6PDx Forward CACAGTGGACGACATCCGAAA	Harvard Primer Bank	N/A
G6PDx Reverse GCAGGGCATTTCATGTGGCT	Harvard Primer Bank	N/A
GCLM Forward AGGAGCTTCGGGACTGTATCC	Harvard Primer Bank	N/A
GCLM Reverse GGAAACTCCCTGACTAAATCGG	Harvard Primer Bank	N/A
PGD Forward AAGCTGACATTGCACTGATCG	Harvard Primer Bank	N/A
PGD Reverse CGGCGGGCTTCTTTAGTT	Harvard Primer Bank	N/A
CXCL10 Forward CCAAGTGCTGCCGTCATTTTC CCAAGTGCTGCCGTCATTTTC	Harvard Primer Bank	N/A
CXCL10 Reverse GGCTCGCAGGGATGATTTCAA	Harvard Primer Bank	N/A
IL6 Forward CTGCAAGAGACTTCCATCCAG	Harvard Primer Bank	N/A
IL6 Reverse AGTGGTATAGACAGTCTGTGG	Harvard Primer Bank	N/A

REAGENT or RESOURCE	SOURCE	IDENTIFIER
Morpholinos		
RelA Morpholino AACAGATCGTCCATGGTCAGGGTCC	GeneTools	N/A
Non-targeted (control) Morpholino GGTTACAATCTAAGATCAAACGACG	GeneTools	N/A
Software and Algorithms		
Improvision Volocity	Perkin Elmer	N/A
ZEN 2010 software	Carl Zeiss	N/A
Image Lab	Bio-Rad	N/A
Prism GraphPad	GraphPad Software	N/A
Python 3.6.4	Python Software Foundation	N/A

Author Manuscript

Author Manuscript

Author Manuscript

Author Manuscript